Geochemistry Geophysics Geosystems G3
AN ELECTRONIC JOURNAL OF THE EARTH SCIENCES
Published by AGU and the Geochemical Society

Article
Volume 3
January 10, 2002
Paper number 2001GC000168
ISSN: 1525-2027

A comparison of tomographic and geodynamic mantle models

Thorsten W. Becker and Lapo Boschi
Department of Earth and Planetary Sciences, Harvard University, 20 Oxford Street, Cambridge, Massachusetts 02138, USA (becker@eps.harvard.edu)

[1] **Abstract:** We conduct a comprehensive and quantitative analysis of similarities and differences between recent seismic tomography models of the Earth's mantle in an attempt to determine a benchmark for geodynamic interpretation. After a spherical harmonic expansion, we find the spectral power and radial correlation of each tomographic model as a function of depth and harmonic degree. We then calculate the correlation, at the same depths and degrees, between all possible pairs of models, to identify stable and model-dependent features (the former being usually of longer spatial wavelength than the latter). We can therefore evaluate the degree of robust structure that seismologists have mapped so far and proceed to calculate ad hoc mean reference models. Tomographic models are furthermore compared with two geodynamic subduction models that are based on plate motion reconstructions. We find systematically low intermediate-wavelength correlation between tomography and convective reconstruction models and suggest that the inadequate treatment of the details of slab advection is responsible. However, we confirm the presence of stable, slab-like fast anomalies in the mid-mantle whose geographic pattern naturally associates them with subduction. This finding, in addition to our analysis of heterogeneity spectra and the absence of strong minima in the radial correlation functions besides the one at ~700 km, supports the idea of whole mantle convection with slab penetration through the 660 km phase transition, possibly accompanied by a reorganization of flow.

Keywords: Tomography; seismic structure; subduction history; mantle convection; correlation analysis.

Index terms: Core and mantle; dynamics, convention currents and mantle plumes; dynamics of lithosphere and mantle general; Earth's interior-composition and state.

Received April 10, 2001; **Revised** July 24, 2001; **Accepted** July 25, 2001; **Published** January 10, 2002.

Becker, T. W., and L. Boschi, 2001. A comparison of tomographic and geodynamic mantle models, *Geochem. Geophys. Geosyst., 3*, 10.129/2001GC000168, 2002.

1. Introduction

[2] Over the last two decades, numerous tomographic models of the Earth's interior have been derived from different types of seismological measurements and with different techniques [e.g., *Dziewonski et al.*, 1977; *Masters et al.*, 1982; *Dziewonski*, 1984; *Inoue et al.*, 1990; *van der Hilst et al.*, 1997]. These models can be seen as snapshots of the convecting mantle, thereby providing important constraints on the planet's dynamics [e.g., *Hager et al.*, 1985; *Mitrovica and Forte*, 1997]. Here we conduct a comparison between global three-dimensional (3-D) mantle models, derived from seismological data, and theoretical geodynamical models. In order

to proceed from mapping heterogeneity to testing geologically relevant hypotheses, such an undertaking is needed for a number of reasons:

1. Discrepancies between tomographic models often arise from differences in the modeling procedure [e.g., *Boschi and Dziewonski*, 1999]. Using a systematic computation of the correlation between different models, we attempt to distinguish stable features from those that depend on data selection and technical choices.

2. Three-dimensional models of compressional (*P*) and shear (*S*) wave velocity in the Earth's mantle are derived from independent observations. The existence of a correlation between *P* and *S* velocity anomalies might mean that they have a common origin, generally believed to be thermal and associated with mantle convection; however, where uncorrelated *P* and *S* velocity heterogeneities are found, compositional heterogeneity can be invoked [e.g., *Su and Dziewonski*, 1997; *Kennett et al.*, 1998]. It is therefore important to specifically measure the correlation between *P* and *S* models.

3. Several authors have attempted to reconstruct the convective flow of the mantle [e.g., *Ricard et al.*, 1993; *Lithgow-Bertelloni and Richards*, 1995, 1998; *Bunge et al.*, 1998; *Bunge and Grand*, 2000; *Steinberger*, 2000a, 2000b] and their results have been used to explain the current pattern of seismic heterogeneities. However, there is still some controversy on this subject; debated issues include the extent to which the phase transition at 660 km represents a barrier to mantle flow [e.g., *van der Hilst et al.*, 1997; *Puster and Jordan*, 1997] and whether a layer or other large-scale structures exist in the deep mantle [e.g., *van der Hilst and Kárason*, 1999; *Tackley*, 2000]. To contribute to this discussion, we carry out a quantitative comparison of seismological versus geodynamic results with the same algorithm used to find the correlation between tomographic models.

[3] More than any previous comparative interpretation of global tomography [e.g., *Grand et al.*, 1997; *Masters et al.*, 1999] and geodynamics [e.g., *Lithgow-Bertelloni and Richards*, 1998; *Bunge et al.*, 1998], our study includes a comprehensive, consistent, and quantitative analysis of all recently published models, allowing the reader to make an informed choice as to which features and geodynamic inferences can be considered robust. The additional online material, which can be found at http://www.geophysics.harvard.edu/geodyn/tomography, makes all correlation and power spectra plots as well as model data available in a convenient form.

[4] We follow *Masters et al.* [1999] and choose to measure the similarity between models in terms of the linear correlation between their spherical harmonic expansions. Only with a spectral analysis are we able to identify wavelength-dependent features and detect changes in the character of the spectrum of imaged heterogeneity (section 4.1.1). Our global measure of correlation suffers from certain drawbacks [e.g., *Ray and Anderson*, 1994], especially when narrow signals such as subducting slabs are studied. Wavelets might be better able to detect local features [e.g., *Bergeron et al.*, 2000]; in section 4.3 we circumvent these problems with an additional spatial domain analysis.

[5] It is our finding that the correlation between modern global tomographic models is high at long wavelengths, even when *P* and *S* wave models are compared with each other; in particular, slab-like structures extending below the 660 km phase transition are a stable feature of all models, and no other radial discontinuity is required at larger depths. Tomographic models are less similar at shorter wavelengths, and on a global intermediate-wavelength scale, do not yet correlate well with the slab signal of geodynamic models.

2. Models

[6] Following is a brief description of all the models we study.

2.1. P Wave Tomography

[7] MIT model hwe97p is parameterized in terms of 2° × 2° blocks of variable radial extent [*van der Hilst et al.*, 1997] and is undefined in areas where the data coverage was considered inadequate ("gaps").

[8] Model kh00p is derived similarly to hwe97p, but a coarser parameterization (3° × 3° blocks) and additional travel time data (from "core-phases") has led to a model that is defined everywhere in the mantle [*Kárason and van der Hilst*, 2001].

[9] Model bdp98 denotes the Harvard equal area block model BDP98 (5° × 5° at the equator, constant radial extent of ~200 km) [*Boschi and Dziewonski*, 1999].

[10] Model bdp00 is an unpublished improvement of bdp98 based on further relocation efforts [see *Antolik et al.*, 2001].

[11] All *P* wave models are based on body wave travel time measurements collected by the International Seismological Centre (ISC). ISC data can be improved by source relocation; this has been done by both the Harvard group [*Su and Dziewonski*, 1997] and with a different method by *Engdahl et al.* [1998]. Both MIT models were derived from *Engdahl et al.*'s [1998] data set.

2.2. S Wave Tomography

[12] Love and Rayleigh waves are mostly sensitive to anomalies in horizontally and vertically polarized shear velocity, v_{sh} and v_{sv}, respectively, and only marginally affected by perturbations in *P* velocity, v_p [e.g., *Anderson and Dziewonski*, 1982]. Observations of surface waves are therefore usually taken into account in deriving *S* models, while v_p heterogeneities are only constrained by the travel times of body waves whose ray geometry is generally nearly vertical within the upper mantle. As a result, the data coverage for v_s in the upper mantle is much more uniform than for v_p.

[13] Model grand is the equal-area block model as of Grand's ftp-site in fall 2000 [see *Grand et al.*, 1997], distributed on a 2° × 2° grid. The model was derived from a combination of body and surface wave measurements with a two step process [*Grand*, 1994]: first, observations are explained in terms of upper and lowermost mantle structure only. Second, the authors invert the residual travel-time anomalies to find velocity heterogeneities in the rest of the mantle.

[14] Model ngrand is an updated version of grand, as of Grand's ftp-site in June 2001. The inversion that led to ngrand was damped more strongly in the upper mantle than that of grand (S. Grand, personal communication, 2001); as a result, the new model is different from grand mostly in amplitude, rather than pattern, of heterogeneity (see 4.1.2).

[15] Here s20rts denotes the Caltech model S20RTS, parameterized horizontally in terms of spherical harmonics up to degree $\ell_{\max} = 20$ and radially with a set of cubic splines [*Ritsema and van Heijst*, 2000]. The model is derived from a data set that, in addition to body and Rayleigh wave measurements, includes observations of normal mode splitting functions.

[16] Here saw24b16 describes the Berkeley v_{sh} model SAW24B16 [*Mégnin and Romanowicz*, 2000], derived by fitting body and surface wave transverse-component waveforms. Parameterized with spherical harmonics ($\ell_{\max} = 24$) and cubic splines.

[17] Model sb4l18 denotes the Scripps model SB4L18, from observations of body, Love, and Rayleigh waves, and normal modes [*Masters et al.*, 1999]. Parameterized in terms of equal-area blocks (4° × 4° at the equator) with 18 radial layers.

[18] Model s20a stands for the Harvard model S20A from observations of body, Love, and Rayleigh waves [*Ekström and Dziewonski*, 1998]. The v_{sh} and v_{sv} anomalies were treated as independent free parameters; v_s is subsequently estimated from their Voigt average. Spherical harmonics representation ($\ell_{\max}$ = 20) is used horizontally; radially, upper and lower mantle are parameterized separately with two sets of Chebyshev polynomials.

[19] Here s362d1 denotes the Harvard model S362D1, derived with a procedure analogous to s20a (including the discontinuity at 660 km) but described by a cubic spline parameterization both horizontally and vertically [*Gu et al.*, 2001]. Lateral resolution is equivalent to $\ell_{\max} \sim 18$.

[20] In addition, we will also use lower resolution joint inversions for v_s and v_p in section 4.2.3. We consider MK12WM13 [*Su and Dziewonski*, 1997] (spherical harmonics, $\ell_{\max} = 12$, Chebyshev polynomials with depth, v_p and v_s anomalies denoted by mk12wm13p and mk12wm13s, respectively), SB10L18 by *Masters et al.* [2000] (similar to sb4l18 but $10^\circ \times 10^\circ$ blocks, pb10l18 and sb10l18), and Harvard model SPRD6 from normal mode splitting coefficients [*Ishii and Tromp*, 2001] (spherical harmonics, $\ell_{\max} = 6$, sprd6p and sprd6s).

2.3. Mean Tomography Models

[21] While most tomographic models present significant discrepancies, they agree on certain, long-wavelength patterns. Efforts to define a 3-D reference Earth model from an inversion of geophysical observables are currently under way (see, e.g., the Reference Earth Model (REM) web site, http://mahi.ucsd.edu/Gabi/rem.html). A REM would be a starting point for higher resolution models and provide the much needed benchmark to evaluate geodynamical hypotheses. Here we adopt a pragmatic approach and calculate two mean models by taking a weighted average of several models, assuming that such "stacking" will enhance the "signal-to-noise" ratio (see appendix B). The result is a largest common denominator model which we intend to update as tomographic research progresses. Model pmean is our mean *P* wave model based on bdp00 and kh00p. Model smean denotes our mean *S* wave model, based on ngrand, s20rts, and sb4l18.

2.4. Geodynamic Models

[22] We compare the previous velocity models with an upper mantle slab model, two geodynamic models that account for inferred past subduction, and, in a statistical sense, with a 3-D thermal convection calculation.

[23] Model rum is our spherical harmonic expansion of slabs in the upper mantle obtained from the RUM seismicity contours [*Gudmundsson and Sambridge*, 1998], which are in turn based on the *Engdahl et al.* [1998] catalog. We integrate along the RUM contours at each layer using them as δ-functions such that the effective width of the slabs is determined by $\ell_{\max}$ and the $\cos^2$-taper that we apply for $\ell > 0.75\ell_{\max}$.

[24] Model lrr98d denotes the density model by *Lithgow-Bertelloni and Richards* [1998] which is given on spherical harmonics laterally ($\ell_{\max}$ = 25) and layers with depth. Model lrr98d is based on "slablets," i.e., negative buoyancy anomalies that sink at different speeds in the upper and lower mantle after starting at estimated past trench locations which are based on Mesozoic and Cenozoic plate reconstructions [*Lithgow-Bertelloni et al.*, 1993; *Ricard et al.*, 1993]. The sinking rate was adjusted to fit geopotential fields, tomography, and plate motions.

[25] Model stb00d describes the density model by *Steinberger* [2000b], which is given on spherical harmonics ($\ell_{\max}$ = 31) and radial layers. Model stb00d is also based on past plate motions and subduction; *Lithgow-Bertelloni et al.*'s [1993] sets of plate boundaries were,

however, interpolated at 2 Ma intervals, while *Lithgow-Bertelloni and Richards* [1998] held boundaries fixed during individual plate-tectonic stages. Model stb00d is furthermore different from lrr98d in that it allows for lateral advection of slablets once they are below 380 km due to the flow that is generated by plate motion and slab buoyancy. Model stb00d can be considered more realistic than lrr98d with respect to the treatment of convective flow.

[26] Model zmg00t is a temperature snapshot from a 3-D spherical convection calculation by *Zhong et al.* [2000]. We use the residual (RMS) temperature from their case 7 at time 9.25 $\times 10^{-4}$. Case 7 is an incompressible, temperature and depth-dependent viscosity calculation without phase transitions that allowed for plate-like flow through the inclusion of fixed weak zones [*Zhong et al.*, 2000, Plates 2a and 2b]. Assuming constant thermal expansivity, α, variations in nondimensional temperature, $\overline{T}$, relate to density, ρ, as $d \ln \rho = -\alpha\Delta\ d\overline{T}$. With $\Delta T = 1800°$ for the nonadiabatic mantle gradient and $\alpha = 1.4 \times 10^{-5}$ K^{-1}, we scale with $\alpha\Delta T \approx 0.025$.

[27] Current and past plate motions are some of the best indicators for the style of convective flow in the mantle. The derived slab sinker trajectories and density distributions of models such as stb00d should thus be among the best constrained geodynamic models. However, given the discrepancies that we observe between lrr98d and stb00d (see section 4.3), we will not attempt to explore thermal convection models [e.g., *Tackley*, 1996; *Bunge et al.*, 1998; *Zhong et al.*, 2000] in greater detail at this point but only complement power spectra of tomography with one representative pattern from zmg00t (section 4.1.1).

3. Measures of Model Correlation

[28] Before carrying out any comparisons, we must find a consistent description. As tomographic models are expressed with respect to different 1-D reference profiles, we first scale heterogeneity to relative deviations from the preliminary reference Earth model (PREM) [*Dziewonski and Anderson*, 1981] and define

$$\delta v_{p,s} = d \ln v_{p,s} = \frac{dv_{p,s}}{v_{p,s}}. \quad (1)$$

[29] We then evaluate each model at a discrete set of depths z_i (i = 1,2,..., N); at each z_i, we find the coefficients of a spherical harmonic expansion of the model, as a function of θ and ϕ, up to degree $\ell_{\max}$ = 31 (see section 3.1). We set to zero all the ℓ = 0 coefficients, corresponding to the constant offset from PREM at each depth. Correlation is usually computed for each harmonic degree up to ℓ = 20, which is the nominal resolution limit of most long wavelength models (corresponding to a half wavelength of ~1000 km at the surface).

3.1. Spherical Harmonic Expansion

[30] Using unity-norm real spherical harmonics [e.g., *Dahlen and Tromp*, 1998, B.8], we approximate any given field $\delta v(\theta, \phi)$ of velocity or density anomalies at a given depth with its expansion up to $\ell_{\max}$,

$$\delta v(\theta, \phi) \approx \sum_{l=0}^{\ell_{\max}} \left[a_{\ell 0} X_{\ell 0}(\theta) + \sqrt{2} \sum_{m=1}^{\ell} X_{\ell m}(\theta) \times (a_{\ell m} \cos m\phi + b_{\ell m} \sin m\phi) \right], \quad (2)$$

where $X_{\ell m}$ are the normalized associated Legendre functions. The set of coefficients $\{a_{\ell m}, b_{\ell m}\}$ is found by

$$a_{\ell 0} = \int_\Omega d\Omega\, X_{\ell 0}(\theta) \delta v(\theta, \phi) \quad \text{for} \quad m = 0 \quad (3)$$

and

$$\begin{pmatrix} a_{\ell m} \\ b_{\ell m} \end{pmatrix} = \sqrt{2} \int_\Omega d\Omega \left(X_{\ell m}(\theta) {\cos m\phi \atop \sin m\phi} \right) \delta v(\theta, \phi) \quad \text{for} \quad 1 \le m \le \ell, \quad (4)$$

where $\int_\Omega d\Omega$ indicates integration over the unit sphere. Our experiments with different numerical integration methods and smoothly interpolated grids with spacings between 0.5° and 2° indicate that the spurious power which is introduced by the expansion of block models should be smaller than ~2.5% for degrees $\ell \leq 20$.

[31] Some tomography models are undefined in areas where the ray coverage was considered inadequate. The effect of these gaps is most extreme for hwe97p, where the areal coverage varies between ~40% at the surface and ~95% at the core mantle boundary (CMB). Since the size of gaps can be large, we set the velocity perturbations to zero in those regions before computing (3) and (4). This choice has the same effect as the imposition of a strong norm-minimization constraint in a least squares fit of $\{a_{\ell m}, b_{\ell m}\}$ (i.e., underestimation of RMS heterogeneity). While this approach is not ideal, we think that a more elaborate treatment is unnecessary since the gapless kh00p has replaced hwe97p, and we will not base any of our conclusions upon hwe97p. Gaps in grand and ngrand occupy a fraction smaller than 1.1% and 0.3% at all depths, respectively; in these cases we have interpolated using the "surface" algorithm [*Wessel and Smith*, 1991] before expanding the fields.

3.2. Power as a Function of Wavelength

[32] We define the spectral power of the field $\delta v(\theta, \phi)$ per degree ℓ and unit area as [e.g., *Dahlen and Tromp*, 1998, B.8]:

$$\sigma_\ell^2 = \frac{1}{2\ell+1}\sum_{m=0}^{\ell}\left(a_{\ell m}^2 + b_{\ell m}^2\right), \tag{5}$$

such that a δ - function results in a flat spectrum (depth dependence will be assumed implicitly). The root-mean-square (RMS) power of the expansion is then

$$\delta v_{\mathrm{RMS}} \approx \frac{1}{\sqrt{4\pi}}\sigma_{\mathrm{RMS}} = \sqrt{\frac{1}{\sqrt{4\pi}}\sum_{\ell=1}^{\ell_{\max}}(2\ell+1)\sigma_\ell^2} \tag{6}$$

since

$$\int_\Omega [\delta v(\theta,\phi)]^2 d\Omega = \sum_{\ell=0}^{\infty}\sum_{m=0}^{\ell}\left(a_{\ell m}^2 + b_{\ell m}^2\right). \tag{7}$$

We note that other definitions of spectral power can be found in the literature [e.g., *Su and Dziewonski*, 1991]; our choice (normalization by $2\ell + 1$ in (5)) emphasizes the wavelength dependence of heterogeneity.

3.3. Cross-Model Correlation

[33] To evaluate the similarity of any two models at a given depth, we find the correlation r^ℓ between the spherical harmonic expansions $\{a_{\ell m}, b_{\ell m}\}$ and $\{c_{\ell m}, d_{\ell m}\}$ of the corresponding fields at each wavelength ℓ,

$$r^\ell = \frac{\sum_{m=0}^{\ell}\left(a_{\ell m}c_{\ell m} + b_{\ell m}d_{\ell m}\right)}{\sqrt{\sum_{m=0}^{\ell}\left(a_{\ell m}^2 + b_{\ell m}^2\right)}\sqrt{\sum_{m=0}^{\ell}\left(c_{\ell m}^2 + d_{\ell m}^2\right)}}. \tag{8}$$

[34] The total correlation up to $\ell_{\max}$ is given by

$$r_{\ell_{\max}}^{tot} = \frac{\sum_{\ell=1}^{\ell_{\max}}\sum_{m=0}^{\ell}\left(a_{\ell m}c_{\ell m} + b_{\ell m}d_{\ell m}\right)}{\sigma_{\mathrm{RMS}}^{\{a_{\ell m},b_{\ell m}\}}\sigma_{\mathrm{RMS}}^{\{c_{\ell m},d_{\ell m}\}}}. \tag{9}$$

where $\sigma_{\mathrm{RMS}}^{\{a_{\ell m},b_{\ell m}\}}$ and $\sigma_{\mathrm{RMS}}^{\{c_{\ell m},d_{\ell m}\}}$ denote the RMS sums for each model. We have verified that the spectral formula (9) yields results that are similar to those found from applications of the common spatial description (see appendix C3).

[35] After applying (8) and (9) to find the correlation between every combination of two models at M evenly spaced z_j where the models have been interpolated, we take the weighted average ($0 \leq z_j \leq 2871$ km):

$$\langle r_{\ell_{\max}}\rangle = \frac{\sum_{j=1}^{M} w_j r_{\ell_{\max}}^{\mathrm{tot}}(z_j)}{\sum_{j=1}^{M} w_j} \quad \text{with} \quad w_j = \left(a - z_j\right)^2, \tag{10}$$

where a is the Earth's radius; each layer enters the average according to its volume. While $\langle r\rangle$ is thus biased by shallow structure, our approach seems appropriate for a global measure of similarity and we find that cross-model $\langle r \rangle$ does not depend strongly on this weighting.

[36] Equations (8)–(10) are estimates of the similarity of two models in terms of global heterogeneity patterns; differences in amplitude do not affect r^ℓ or $r^{\mathrm{tot}}_{\ell_{\max}}$ (see appendix A for the statistical interpretation of r). We find and compare r^{tot}_8 and r^{tot}_{20} to evaluate separately the correlation between the long and intermediate spatial wavelength components of the models.

3.4. Radial Parameterization

[37] We generally attempt to remain close to the original radial parameterization of all models: if models were described in terms of discrete layers, we first evaluate them at the original mid-layer depths, z_i. Likewise, we evaluate spline models at, roughly, the original spline knots and models that are parameterized with Chebyshev polynomials at constantly spaced ($\sim$150 km) intervals. Subsequently, if the value of the model is needed at any other depth z_j, we find it by linear interpolation.

[38] To explore how results are affected by different radial parameterizations, we will additionally show results from models that were reparameterized in terms of normalized Chebyshev polynomials of order k [e.g., *Su and Dziewonski*, 1997]. We obtain the Chebyshev coefficients by a least squares fit of the original expansion coefficients at the z_i using a combination of norm and roughness damping. This leads to a smoothed but faithful representation of the original models (see appendix C4): with $k_{\max} = 20$, we have a resolution of $\sim$150 km and achieve variance reductions typically better than 95%.

3.5. Radial Correlation

[39] Following *Puster and Jordan* [1997], we calculate the radial correlation matrix $r(z_1, z_2)$ between the lateral structure of the same model at any two depths z_1 and z_2. (Correlation $r(z_1, z_2)$ is simply the value of $r^{\mathrm{tot}}_{\ell_{\max}}$ found from the expansions $\{a^{z_1}_{\ell m}, b^{z_1}_{\ell m}\}$ and $\{a^{z_2}_{\ell m}, b^{z_2}_{\ell m}\}$ at the depths z_1 and z_2, respectively.) Two derived, closely related measures of radial coherence as a function of z are (1) the correlation coefficient $r(z - \Delta z, z + \Delta z)$ for a fixed depth bracket Δz, and (2) the value of Δz associated with a contour of constant $r(z - \Delta z, z + \Delta z)$.

[40] As outlined by *Puster and Jordan* [1997], radial correlation functions can be interpreted as a measure of mass flux between different depth ranges in the convecting mantle. In practice, we compute $r(z_1, z_2)$ for all z_i and interpolate on a smooth field at $\sim$25 km grid spacing. For models whose spline parameterization density varies with depth, it is difficult to obtain adequate depth spacings; our discrete z_i estimate of the correlation functions suffers therefore from some oversampling, especially for s20rts. The resulting oscillations are, however, easily detected and can be avoided if we choose a Chebyshev parameterization with depth (see appendix C4).

4. Results

4.1. Analysis of Individual Models

[41] We study the spectral signal, δv_{RMS}, and radial correlation of each model before comparing models to one another. For consistency, all values of geodynamic models are scaled by

$$\Lambda = \frac{d \ln v_s}{d \ln \rho} = \frac{\delta v_s}{\delta \rho} = 3.6\,, \qquad (11)$$

a weighted radial average (we neglect depth-dependence of Λ for simplicity) of *Karato*'s [1993] profile.

4.1.1. Power spectra variation with depth

[42] After computing the spectral power per degree $\sigma^2_\ell(5)$, we normalize it by its maximum

at each depth in order to emphasize the dominant wavelengths and denote the resulting quantity $\hat{\sigma}_\ell^2$. The first moment of a weighted sum of $\hat{\sigma}_\ell^2$,

$$M(z) = \frac{\sum_{\ell=1}^{\ell_{\max}} \ell(2\ell+1)\hat{\sigma}_\ell^2(z)}{\sum_{\ell=1}^{\ell_{\max}} (2\ell+1)\hat{\sigma}_\ell^2(z)}, \qquad (12)$$

is a measure of the z dependence of the strongest wavelengths, i.e., the "color" of the heterogeneity spectrum. (Absolute values of $M(z)$ are only meaningful when $\hat{\sigma}_\ell^2 \to 0$ as $\ell \to \ell_{\max}$; most tomographic models approximately satisfy this condition.)

[43] Figure 1 shows the normalized spectrum (see Figure C2 for σ_ℓ^2) and δv_{RMS} (equation (6)) for a selection of tomographic and geodynamic models. Most tomographic models are dominated by long wavelengths ("red," $\ell \leq 5$) at all depths [e.g., *Su and Dziewonski*, 1992]. These low degree patterns roughly correspond to the continent/ocean function at the surface, the circum-Pacific subduction signal in the mid-mantle, and the "mega-plumes" toward the CMB. In other words, mantle convection appears to be organized by plate-scale flow with length scales as observed at the surface [e.g., *Davies*, 1988].

[44] *P* models kh00p and bdp00 have a different spectral character in the uppermost mantle (where $M(z)$ and δv_{RMS} from bdp00 are smoother functions of depth) and for 1600–2400 km depths. In both cases, there is a shift in kh00p's spectrum from degree 2 to degree 1. Furthermore, bdp00 indicates a stronger change in spectral character at $z \sim 800$ km than kh00p. The δv_{RMS} of bdp00 is overall larger in the upper mantle than that of bdp98: most likely a result of *Antolik et al.*'s [2001] source relocation with subsequent improvement of the Harvard data (see the additional online material). The kh00p and bdp00 models are consistent in that the absolute $\ell = 2$ power has a local minimum at $\sim$2000 km depth (Figure C2).

[45] The $\hat{\sigma}_\ell^2$-spectrum of s20rts is dominated by $\ell = 2$ everywhere in the lower mantle but weaker at intermediate ℓ than for the *P* models. Model s20rts' δv_{RMS}, minimum at $\sim$1600 km depth, is focused in the uppermost mantle where $\hat{\sigma}_\ell^2$ is strongest in degrees $\ell = 1$ and $\ell = 5$, as expected in an *S* model with a well-constrained ocean-continent signal [*Su and Dziewonski*, 1991]. The spectrum of s20rts becomes continuously redder with increasing depth starting from $\sim$1500 km. This is a common feature for *S* models while *P* models typically have intermediate wavelength power and a corresponding local maximum in $M(z)$ at $\sim$2000 km. We find a minimum in absolute σ_2^2 for s20rts at $\sim$1600 km (Figure C2), possibly related to the fading slab signal and to the uppermost boundary of the large slow anomalies that reach down to the CMB [*Dziewonski*, 1984]. We also observe that the spectral power of s20rts is consistently higher at even rather than odd ℓ, up to $\ell \sim 12$; one reason for this could be the ℓ-dependence of the sensitivity of normal mode splitting functions (used, among other data, to derive s20rts) to the Earth's structure. However, s20a and the subduction signal in stb00d and lrr98d indicate similar streaks in the power spectrum, while otherwise similar models, such as sb4l18, have no such property (see the additional online material).

[46] The spectrum and δv_{RMS} of s362d1 show the effect of a 660 km deep discontinuity in the radial parameterization: the inversion shifts heterogeneity to the upper mantle and the sub 660 km spectrum gets whiter. *Gu et al.* [2001] find that such variations are not as pronounced when the parameterization discontinuity is placed at other depths. A change in spectral character below 660 km can also be found, to a lesser extent, in other models (e.g., bdp00); it might indicate the effect of a viscosity increase in the lower mantle [e.g., *Mitrovica and Forte*, 1997], leading to reor-

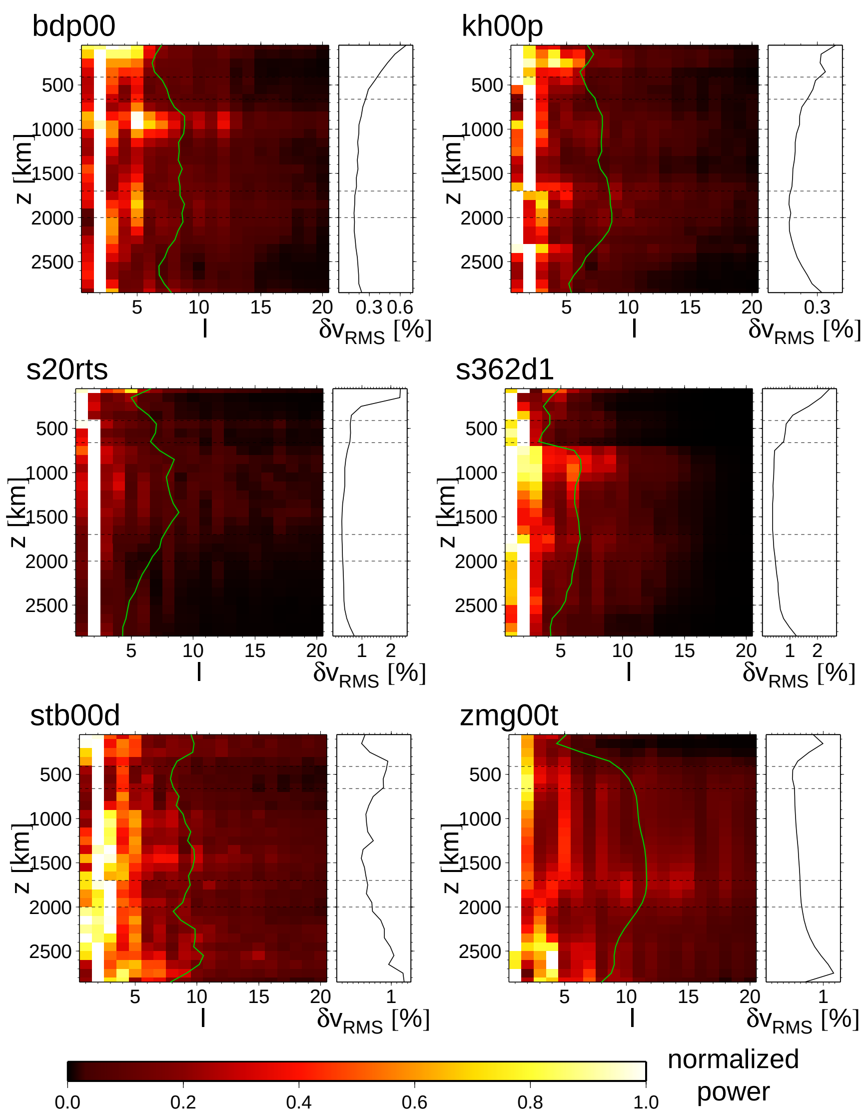

Figure 1. Normalized spectral power, $\hat{\sigma}^2_\ell$ (left subplots) and RMS variations, δv_{RMS} (variable scale with 0.1 tickmarks, right subplots) for *P*, *S*, subduction (stb00d) and thermal convection (zmg00t) models; curve in the left subplot indicates *M*(*z*), equation (12). Dashed lines mark 410 km, 660 km, 1700 km, and 2000 km depths. (Compare Figure C2 and the additional online material.)

ganization of flow and transient slab hold-up (see section 4.1.3).

[47] The $\hat{\sigma}^2_\ell$ of stb00d is strongest for $\ell \lesssim 3$ but differs from tomography in that it has relatively high power over a broad range of wavelengths as expected from the narrow slablet signal. Besides a trend toward a bluer spectrum below 660 km, there is no clear tendency of *M*(*z*) of the subduction signal to vary with depth but, as noted above, we find that even ℓ is stronger in the middle mantle than odd ℓ power for stb00d and lrr98d (see Figures C2 and C6 and the

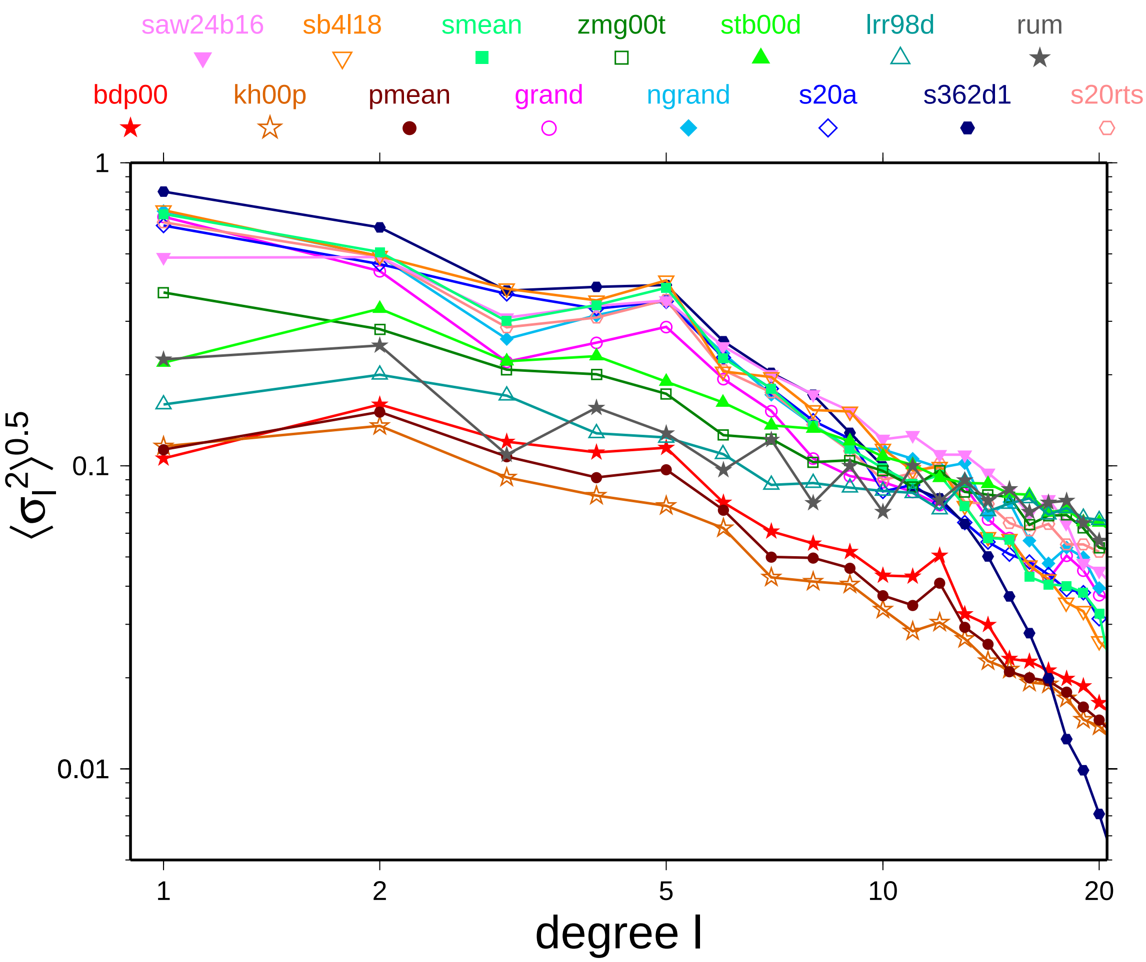

Figure 2. Depth averaged power spectra, $\sqrt{\langle\sigma_\ell^2\rangle}$.

additional online material). Thermal convection model zmg00t is similar to tomography regarding the low degree pattern of heterogeneity. Indeed, case 7 is *Zhong et al.*'s [2000] preferred model since the inclusion of "plates" lead to the characteristic red signal of seismological models in a temperature dependent viscosity calculation. Model zmg00t furthermore resembles tomography in that the signal is bluer in the middle mantle than toward the thermal boundary layers (TBLs, $z \lesssim 500$ km and at the CMB) where δv_{RMS} variations are strongest.

[48] Figure 2 shows depth averaged $\sqrt{\langle\sigma_\ell^2\rangle}$ for a selection of models. In general, *S* models are characterized by stronger heterogeneity than *P* models [e.g., *Anderson*, 1987; *Karato*, 1993] (also see section 4.2.3). As noted above, spectral power for tomography is concentrated at low degrees ($\ell = 1$, $\ell = 2$, with a local maximum at $\ell = 5$) and rapidly decays when $\ell \gtrsim 5$ [e.g., *Su and Dziewonski*, 1991]. Model s362d1 is an outlier, in that it shows the most rapid decrease of $\hat{\sigma}_\ell^2$ for $\ell \gtrsim 12$, mostly owing to a relatively weak high frequency signal in the upper mantle (Figure C2). The geodynamic models stb00d,

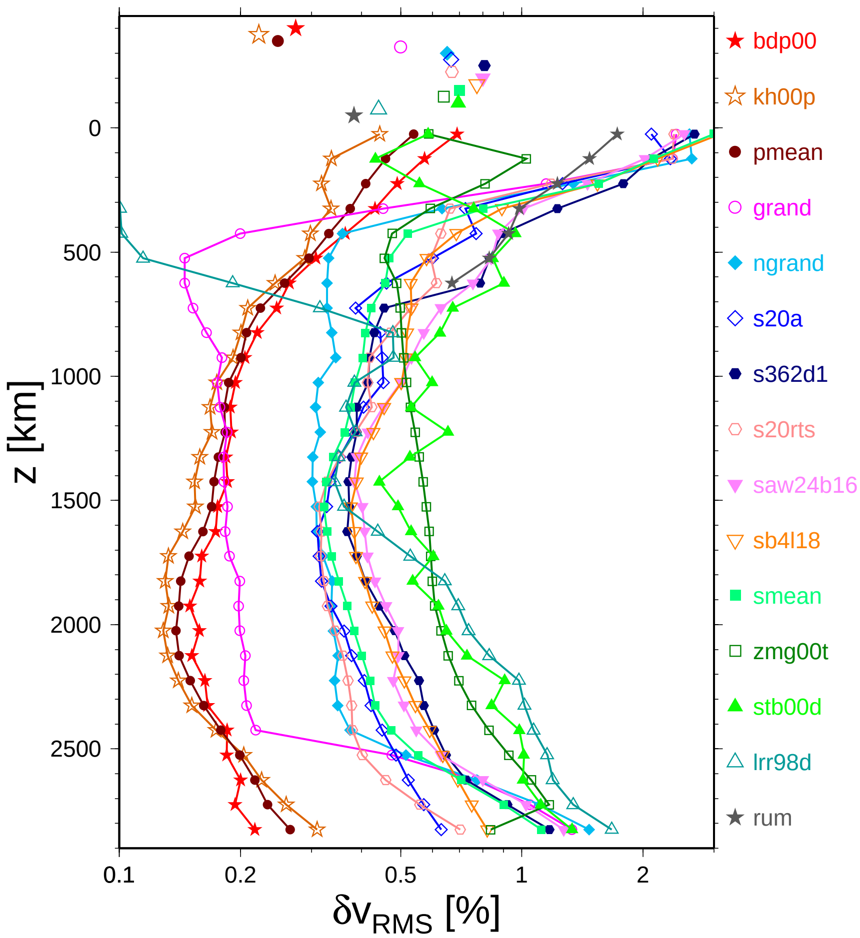

Figure 3. The δv_{RMS} versus z, $\ell_{max} = 31$. Symbols at $z < 0$ denote depth averaged $\langle \delta v_{\mathrm{RMS}} \rangle$.

lrr98d, rum, and zmg00t have a stronger high frequency character than that mapped by tomography.

4.1.2. RMS heterogeneity

[49] The aforementioned concentration of heterogeneity toward the boundary layers of the mantle and the global minima at ∼1600 km (S models) or ∼2000 km (P models) depth are common features of δv_{RMS} as a function of z (Figure 3). In the case of tomographic models, δv_{RMS} is a smooth function of depth; exceptions are grand and ngrand (whose high δv_{RMS} focusing is the result of the inversion procedure), as well as s20a and s362d1 (based on a discontinuous radial parameterization (section 2.2)). Model ngrand is significantly closer in δv_{RMS} to the other S models than its ancestor grand because of modified damping (see section 2.2). As the cross-model correlation between grand and ngrand shows (see the additional online material), patterns were only slightly affected by this modification ($\langle r_{20} \rangle$ = 0.9).

[50] The δv_{RMS} based on subduction models does not agree well with tomography in the

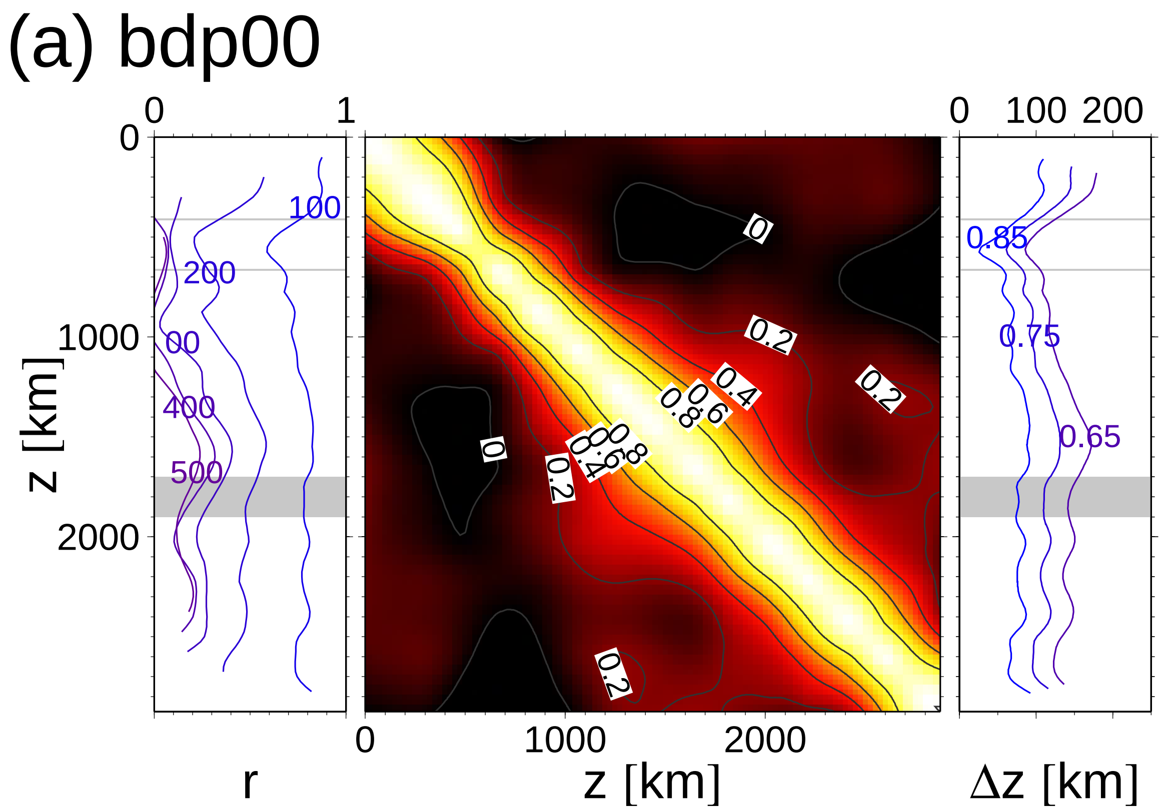

Figure 4. Radial correlation function for (a) bdp00, (b) kh00p, and (c) sb4l18. We show r at fixed Δz of 100–500 km (left plot), the radial correlation matrix $r(z_1, z_2)$ with contours in 0.2 intervals (middle plot, colorscale clipped at 0), and Δz for fixed $r = 0.65$, $r = 0.75$, and $r = 0.85$ (right plot, if we were able to trace a continuous contour). The 410 km, 660 km, and the depth range from 1700 km to 1900 km are indicated.

upper mantle but shows a consistent increase in heterogeneity below ~1500 km. We furthermore find broad agreement between the thermal convection snapshot zmg00t and δv_{RMS} from tomography. However, seismological models indicate stronger variations of δv_{RMS} with z. Also, the upper boundary layer structure is generally more pronounced than the deep one for tomography. Reasons for these discrepancies are the continent/ocean differences and tectosphere (not included in any of the geodynamic models), the fact that $\delta\rho_{\mathrm{RMS}} \rightarrow 0$ at the surface and at the CMB are boundary conditions of zmg00t, and that *Zhong et al.*'s [2000] Rayleigh number is smaller than Earth's by a factor of ~10. We should therefore expect that the TBL thickness is overpredicted and $\overline{T}_{\mathrm{RMS}}$ is underpredicted for zmg00t. Variations in Λ or α (see section 4.1) and other effects such as compressibility will also affect the depth-dependence of δv_{RMS} and the spectrum as predicted by geodynamics [e.g., *Tackley*, 1996]. However, a detailed discussion of dynamic convection models is beyond the scope of this paper.

4.1.3. Radial correlation

[51] Figure 4 shows three measures of the radial correlation of tomographic models: the corre-

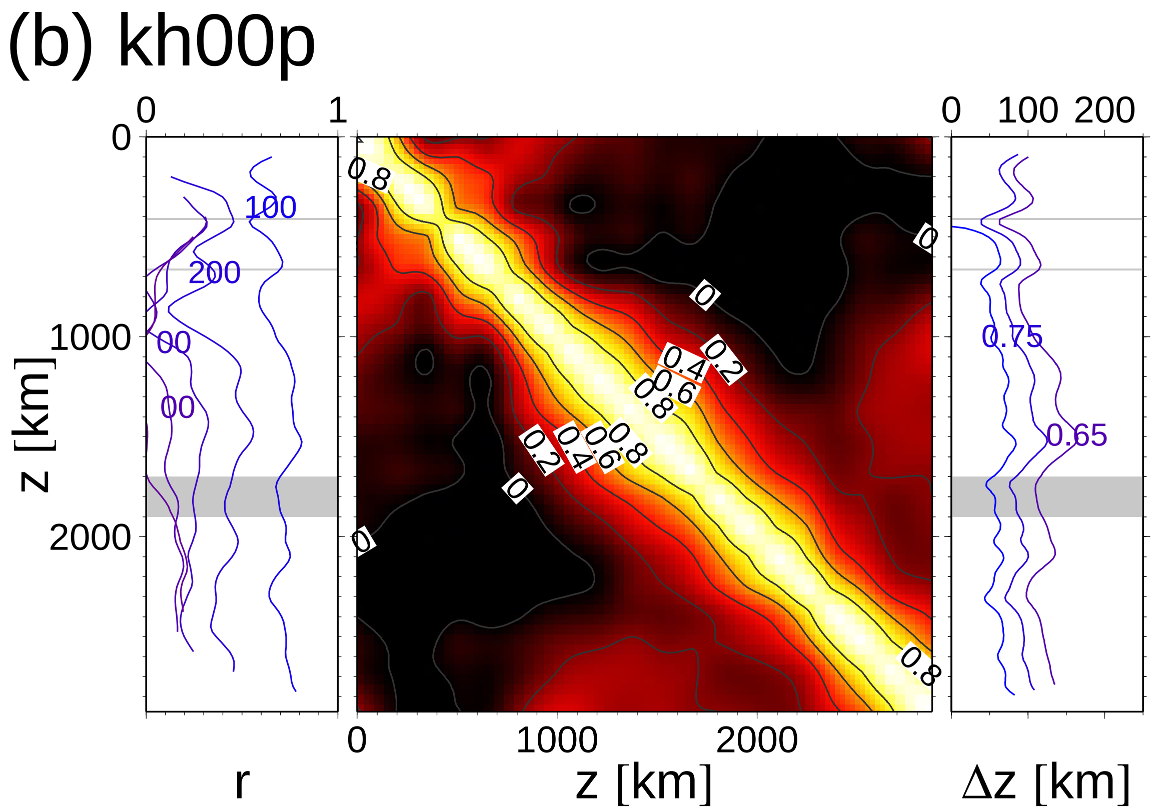

Figure 4. (continued)

lation matrix, Δz at constant $r(z - \Delta z, z + \Delta z)$, and $r(z - \Delta z, z + \Delta z)$ at constant Δz (see section 3.5). All estimates in Figure 4 are based on $\ell_{max} = 20$ expansions (see section C4 for ℓ_{max}-dependence). Model bdp00 (Figure 4a) is characterized by a local minimum in Δz at ~600 km; correlation is then relatively high in the midmantle and decreases toward the CMB. For kh00p (Figure 4b), local minima in radial correlation are found at ~400 km, ~800 km, ~1700 km, and ~2300 km. Our results are similar (but not identical) to those of *van der Hilst and Kárason* [1999] who pointed out the decrease in correlation at ~1700 km. Since estimates of radial correlation are parameterization dependent, we have repeated our calculation for kh00p using the original blocks or a radial Chebyshev reparameterization. The results of this exercise, summarized in section C4, are consistent with Figure 4b.

[52] The radial correlation of *S* models increases with increasing depth (e.g., sb4l18 in Figure 4c, with local minima in Δz at ~300 km and ~600 km). This effect is explained by the general tendency of *S* models to become redder with increasing depth (section 4.1.1): since long-wavelength features are better correlated, we then expect a more homogeneous radial correlation in the lower mantle. Indeed, if we damp out high frequency structure in the *P* models for the lower mantle (typically concentrated at $z \sim 2000$ km), the resulting plots of the radial correlation function resemble those of *S* wave models.

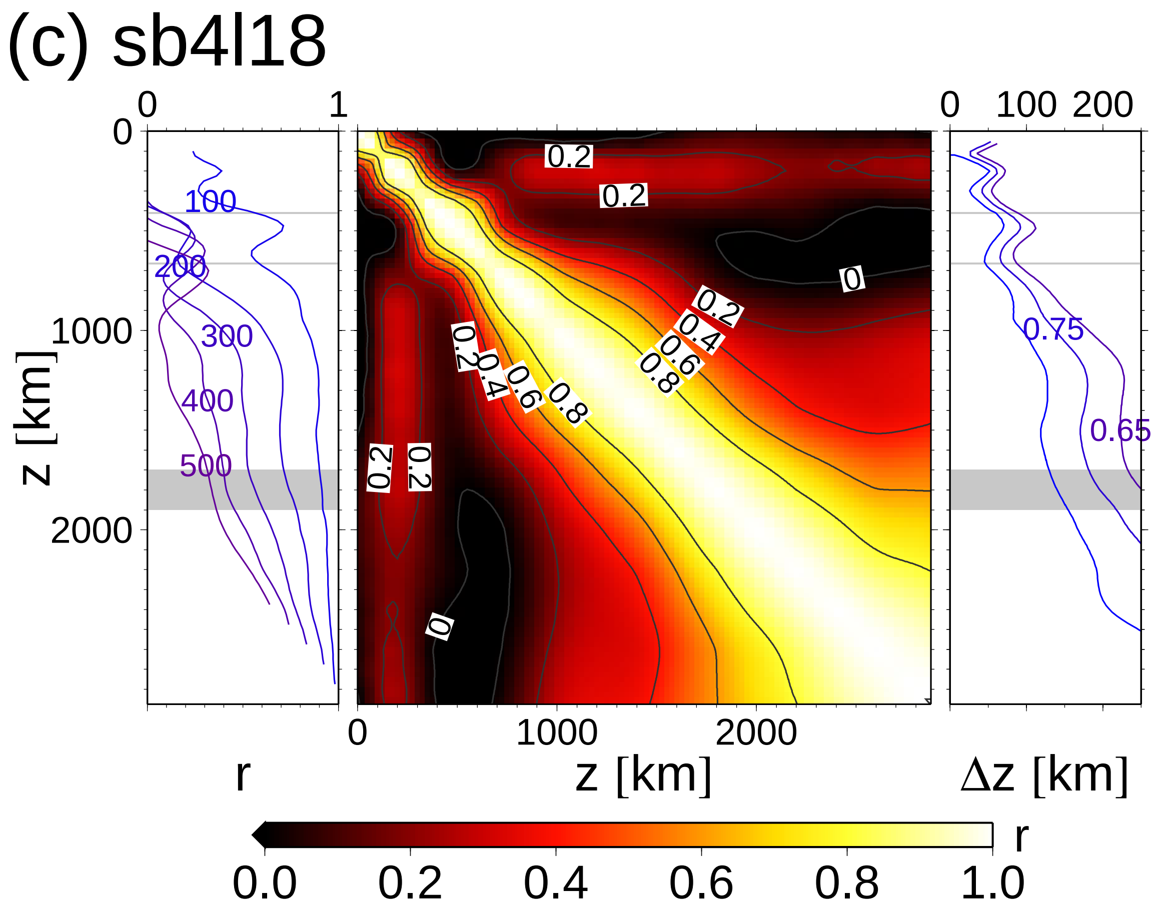

Figure 4. (continued)

[53] We show in Figures 5a and 6a the radial correlation r at Δz = 200 km of a selection of models as it results from our initial calculations with a discrete radial sampling. Then we repeat the calculations after reparameterizing the models over a radial Chebyshev polynomial basis and give the results in Figures 5b and 6b. Consistent features of the P models in Figure 5b are a broad global minimum in correlation for 400 km $\lesssim z \lesssim$ 700 km (possibly with a local maximum at ∼660 km), an increase in r toward 1500 km, and a decrease to a second minimum at 1700 km $\lesssim z \lesssim$ 2400 km. The latter feature is less pronounced in pb10l18 (see the additional online material). As anticipated above, S models (Figure 6) are generally characterized by an increase in r with increasing z. Other notable features are local maxima at ∼660 km, artificial oscillations of the r versus z curve obtained from s20rts (explained in 3.5) and the anomalously large (parameterization related, section 2.2) excursions of s362d1 at 660 km.

[54] Radial correlation estimates vary strongly with model parameterization [e.g., *Ritzwoller and Lavely*, 1995] and power spectra appear to be a more robust estimate of structural change than radial correlation functions. However, we

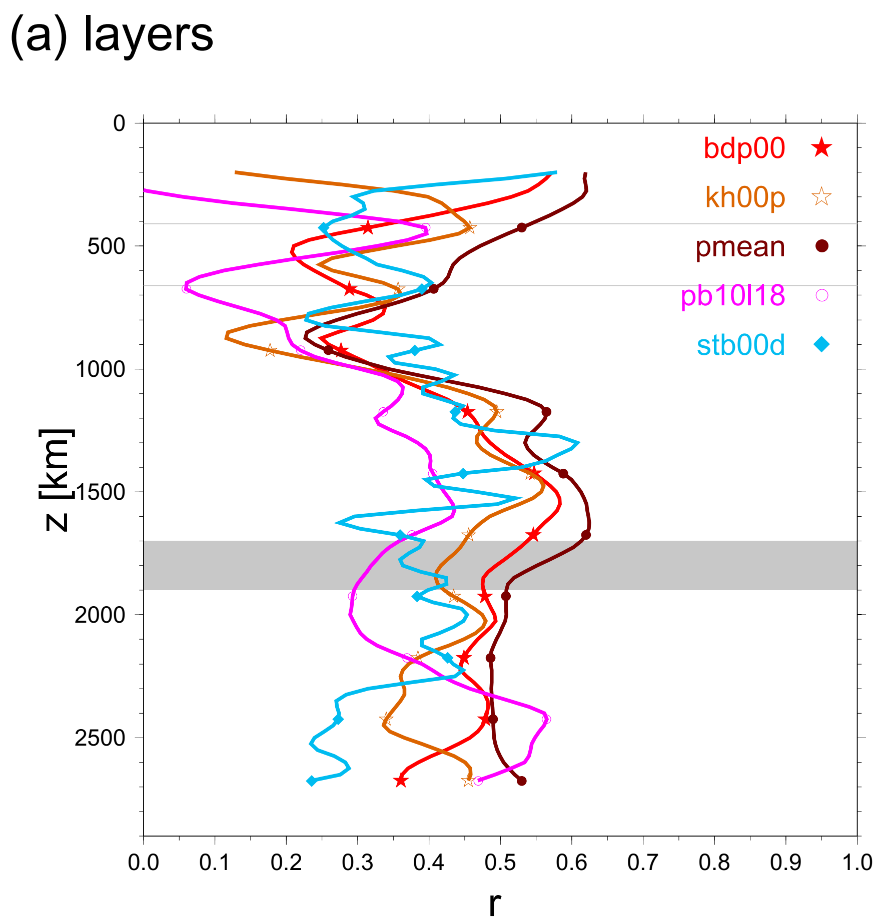

Figure 5. Radial correlation $r(z - \Delta z, z + \Delta z)$ at fixed $\Delta z = 200$ km for (a) P wave tomography with layers and (b) on radial Chebyshev parameterization; stb00d is shown for comparison.

find some indication for low radial correlation in P and S models at ~750 km, and in P models at ~2000 km, previously associated with reorganization of flow and possible deep mantle structure, respectively [*van der Hilst and Kárason*, 1999]. The work of *Puster and Jordan* [1997] and the stb00d (whole mantle flow) derived correlation profiles show that local minima in correlation are not necessarily indicative of a layered style of convection. Changes in slab morphology [e.g., *van der Hilst et al.*, 1997; *van der Hilst and Kárason*, 1999] and the general flow pattern due to the phase transition with a viscosity increase at 660 km [e.g., *Mitrovica and Forte*, 1997] are therefore likely explanations for the first minimum in correlation. Especially transient slab flattening and possible segmentation can be expected to yield apparent structural changes below 660 km as indicated by some of the power spectra that were discussed in section 4.1.1.

[55] The findings that $z \sim 2000$ km is a global minimum of δv_{RMS}, that the radial correlation of S models shows no clear decrease at these depths, and the apparent absence of large scatterers in the lower mantle [*Castle and van der Hilst*, 2000], make the existence of a strong

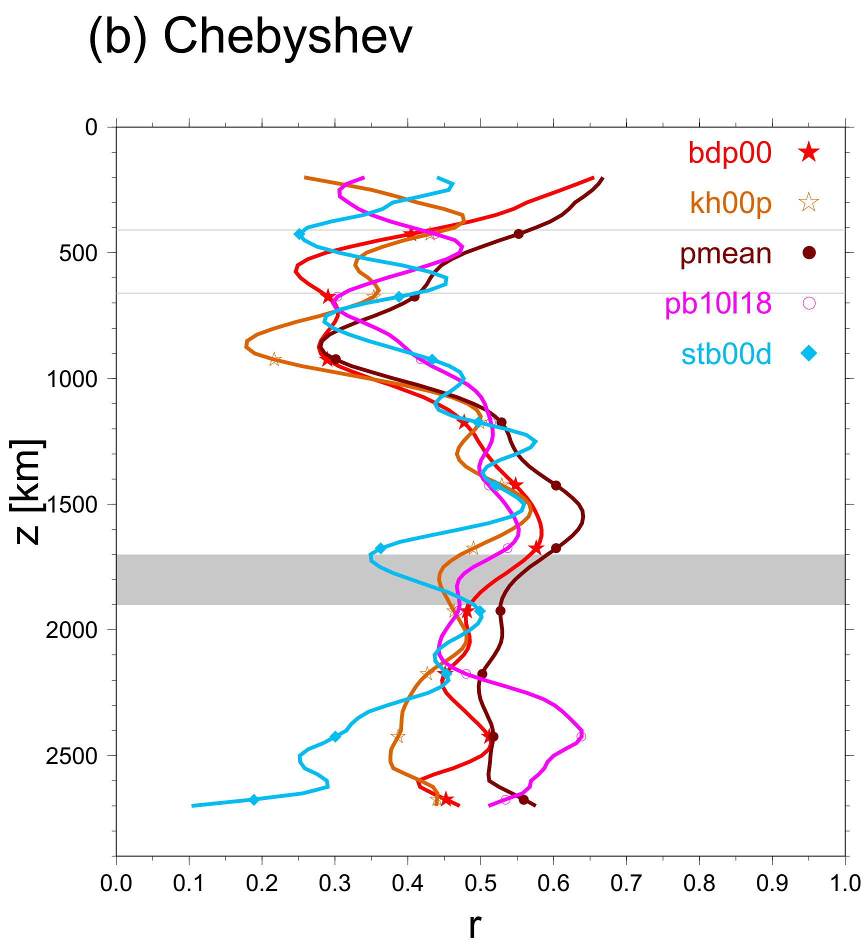

Figure 5. (continued)

global structural change at ~2000 km seem unlikely at this point. However, the local minima in absolute $\ell = 2$ power that we found at ~1700 km (section 4.1.1) are consistent with a fade-out of the slab signal at these depths [e.g., *van der Hilst and Kárason*, 1999; *Kárason and van der Hilst*, 2000] and local structural change [e.g., *Saltzer et al.*, 2001] cannot be ruled out.

4.2. Cross-Model Comparisons

[56] We now quantify similarities and discrepancies between models, focusing on a representative subset. The additional online material includes correlation plots for all possible pairs of models from section 2 with the exception of zmg00t which represents the current state of Earth's mantle only in a statistical sense.

4.2.1. *P* wave models

[57] Figure 7 shows r^{ℓ} between bdp00 and kh00p, an example of the good correlation that generally characterizes *P* models. The pattern and δv_{RMS} of bdp00 and kh00p are mostly consistent throughout the lower mantle and up to $\ell = 20$; significant deviations are found in the uppermost mantle (where δv_{RMS} of kh00p is weaker) and at the CMB (where the inclusion of core phases has enhanced the δv_{RMS} of

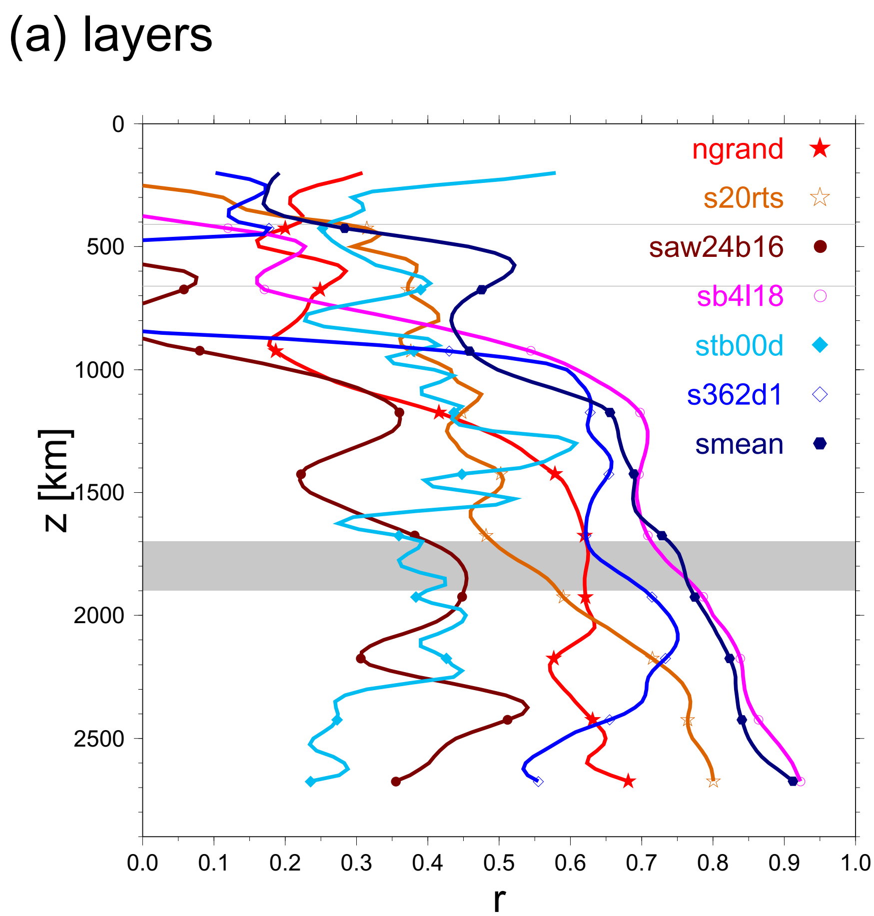

Figure 6. Radial correlation $r(z - \Delta z, z + \Delta z)$ at Δz = 200 km for (a) *S* wave tomography with layers and (b) on radial Chebyshev parameterization. The continuous Chebyshev parameterization is clearly not suited to represent discontinuities in s362d1.

kh00p [*Kárason and van der Hilst*, 2001]). Other local minima in r_8^{tot} and r_{20}^{tot} are at ~300 km, 700 km, and ~1900 km. All three depths show a long wavelength breakdown in correlation ($r_8^{tot} \rightarrow r_{20}^{tot}$), especially at ℓ = 4. The average correlation between bdp00 and kh00p is high ($\langle r_8 \rangle$ = 0.71), to be compared with $\langle r_8 \rangle$ = 0.85 for bdp00–bdp98, and $\langle r_8 \rangle$ = 0.69 for kh00p–hwe97p (but see section 3.1).

4.2.2. *S* wave models

[58] Figure 8 shows r^ℓ for s20rts and sb4l18. Especially at low harmonic degrees, the two models are very consistent, more so than the *P* models in Figure 7. However, at $\ell \gtrsim 12$, correlation degrades such that $\langle r_{20} \rangle$ is slightly lower than for bdp00–kh00p. These intermediate wavelength discrepancies that we find for most *S* models are likely due to the greater variety in input data, while *P* models are inverted from very similar data sets (section 2). The r_8^{tot} and r_{20}^{tot} for Figure 8 have a global maximum near the surface, decrease toward ~1500 km and, as the low-degree portion of the spectrum becomes more important, grow monotonically thereafter while $r_{20}^{tot} \rightarrow r_8^{tot}$.

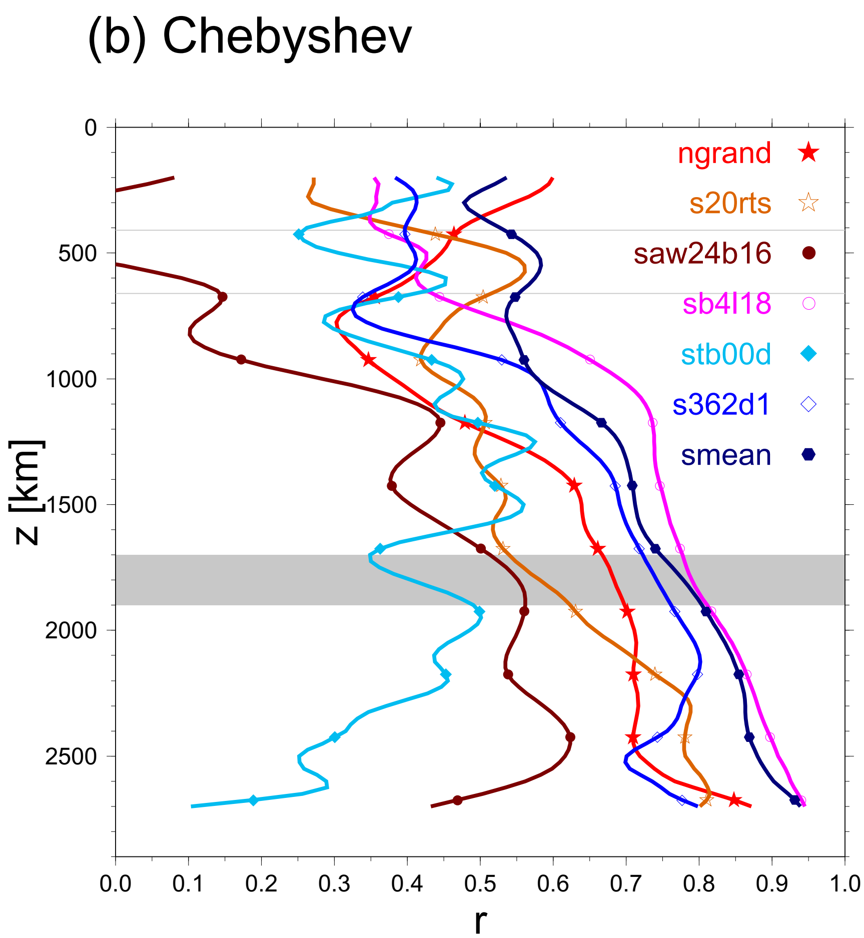

Figure 6. (continued)

[59] The r^{ℓ} behaves as in Figure 8 for most combinations of *S* models (see the additional online material and section 4.2.5). Exceptions are s20a and s362d1: these models correlate well with other *S* models in the upper mantle. Because of their inherent radial discontinuity, however, they are different from other models for 700 km $\lesssim z \lesssim$ 1500 km. Yet, between s362d1 and smean, r^2 and r^3 at z = 800 km are still $\geq$ 0.68 and $\langle r_8 \rangle$ = 0.7. As noted by *Gu et al.* [2001], the data fit of their 660 km discontinuity model was not significantly better than that of their continuous parameterization inversion. This means that discontinuous descriptions of mantle structure are consistent with, but not necessarily required by, the data.

4.2.3. δv_s versus δv_p

[60] Figure 9 is representative of comparisons between models of v_s and v_p. We find that those are generally not as well correlated with each other as models of the same kind. This result can partly be explained by the systematic differences in data distribution and sensitivity, especially in the upper mantle (see section 2.2). The r_{20}^{tot} in Figure 9 shows local minima at $\sim$700 km and at $\sim$1800 km, but only the former is accompanied by a broad $r_8^{\mathrm{tot}} \rightarrow r_{20}^{\mathrm{tot}}$

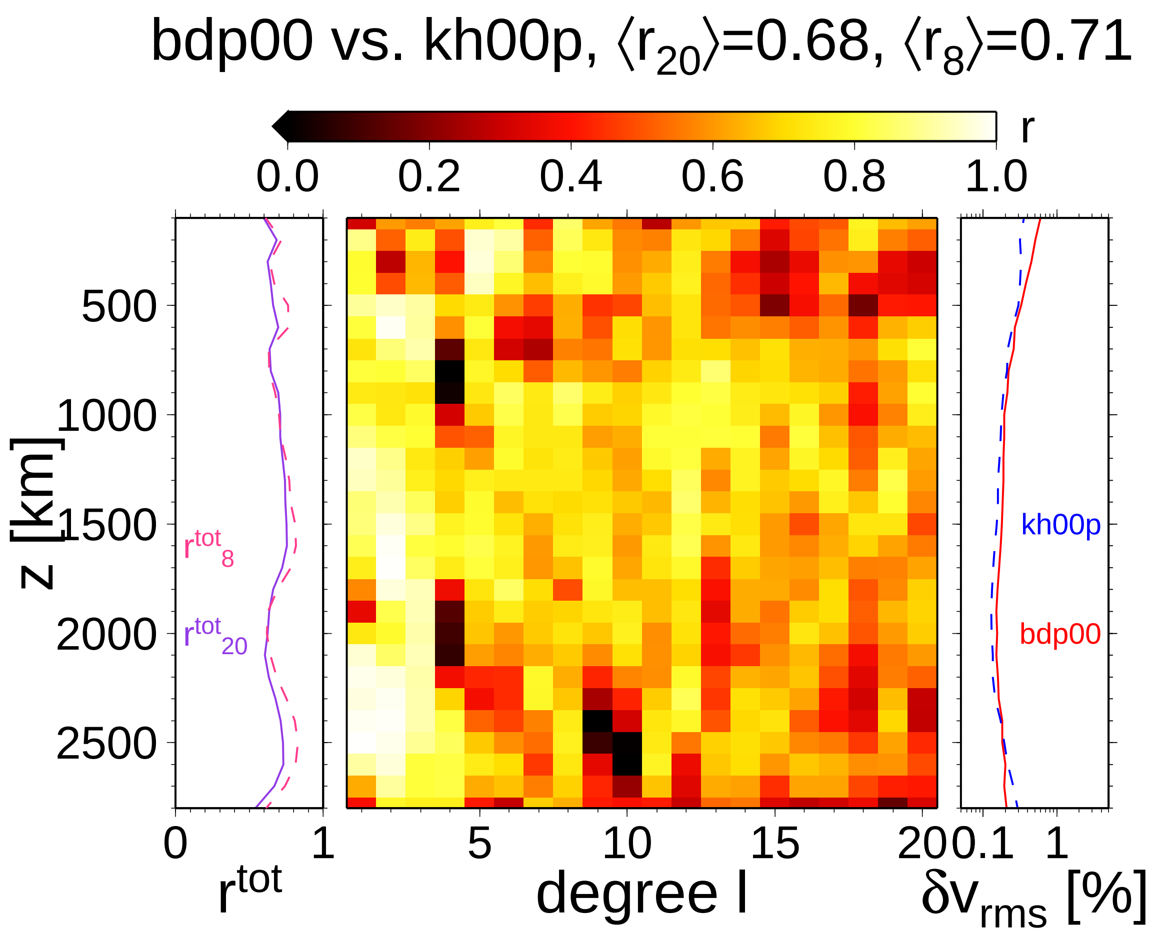

Figure 7. Cross-model correlation between bdp00 and kh00p. We show total correlations r_8^{tot} and r_{20}^{tot} (dashed and solid curves, respectively, left plot), correlations per degree r^ℓ (middle plot), and δv_{RMS} for bdp00 (solid) and kh00p (dashed) on a log-scale (right plot). The colorscale for r^ℓ is clipped at negative values for improved grayscale reproduction; see the additional online material for full colorscale plots.

cross-wavelength breakdown (not as pronounced for comparisons with kh00p).

[61] Figure 10a shows r_{20}^{tot} for a combination of *S* models and bdp00 and kh00p; Figure 10b allows a comparison of our mean models, long-wavelength joint inversions, and the normal mode model SPRD6 (see sections 2.2 and 2.3). We observe that correlation between δv_s and δv_p is low for all models between ~300 km and ~700 km; another minimum is found at ~2000 km for some models. The r_{20}^{tot} between most *P* and *S* models has a local maximum at ~2500 km and then decreases again toward the CMB, hinting at compositional heterogeneity at the bottom of the mantle.

[62] Comparisons of the δv_s–δv_p components of models derived from joint v_s–v_p inversions (Figure 10b) can lead to quite different considerations, depending on the model [*Masters et al.*, 2000]: in the case of MK12WM13, the δv_s–δv_p correlation has a pronounced minimum at ~1000 km and is smaller at low ℓ than at

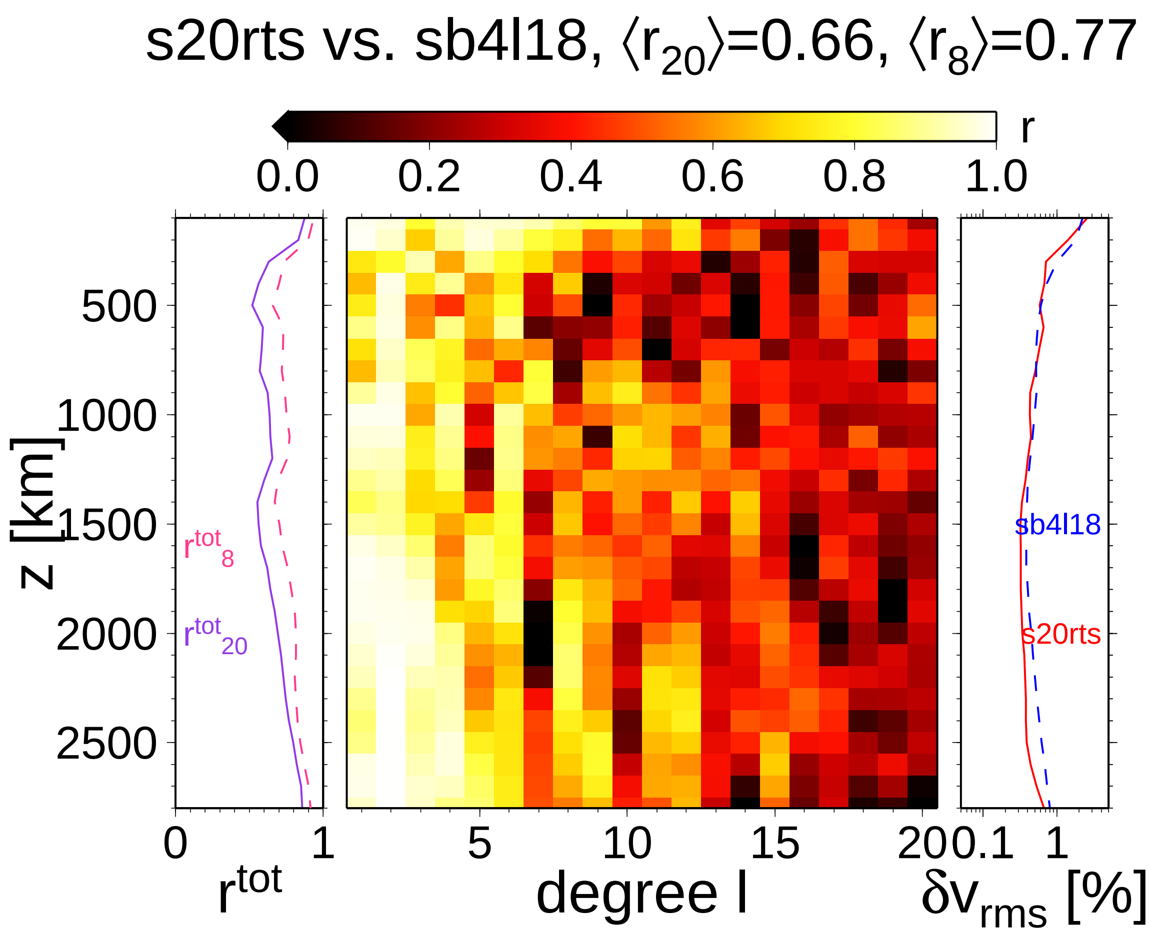

Figure 8. Cross-model correlation for s20rts (solid δv_{RMS}-line) and sb4l18 (dashed δv_{RMS}-line). See Figure 7 for description.

intermediate ℓ. The correlations of smean versus pmean and δv_s versus δv_p components of SB10L18, in contrast, are consistent, with local minima at at $\sim$400 km and $\sim$2000 km (as before, only the former shows $r_8^{\mathrm{tot}} \rightarrow r_{20}^{\mathrm{tot}}$). Absolute correlations are, however, higher for SB10L18.

[63] We next determine

$$R = \frac{d \ln v_s}{d \ln v_p} = \frac{\delta v_s}{\delta v_p}, \tag{13}$$

first from the RMS heterogeneity ratio of the models (solid lines in Figures 10a and 10b, mean $\langle R \rangle$ indicated on the R axis at the CMB). Second, we calculate R from a linear regression of the expansion coefficients of the models at each depth ($\ell_{\max} = 20$); an estimate whose reliability can be judged from the corresponding r_{20}^{tot}. In the absence of information about model uncertainties, R will vary depending on the assumed standard deviations, Σ, of each model. We therefore show a range of best-fit R values from an iterative linear regression [e.g., *Press et al.*, 1993, p. 666] where Σ of the S model, $\Sigma_{\delta v_s}$, is assumed to be twice that of the P model (leading to lower estimates for R) or vice versa, where $\Sigma_{\delta v_p} = 2\Sigma_{\delta v_s}$ (leading to

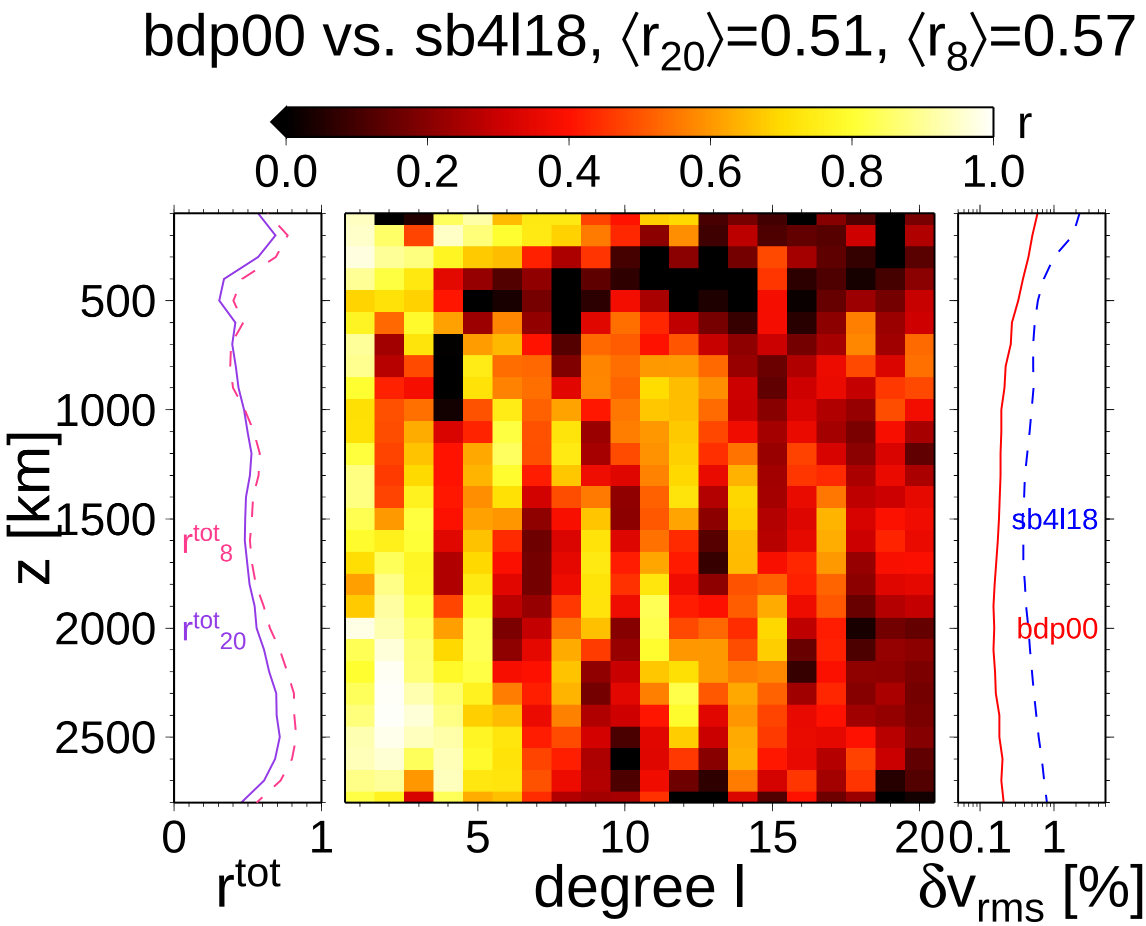

Figure 9. Cross-model correlation for bdp00 (solid δv_{RMS}-line) and sb4l18 (dashed δv_{RMS}-line). See Figure 7 for description.

higher estimates). The corresponding $\langle R \rangle$ values are indicated with different size symbols on the upper R axis in Figure 10a and 10b. For comparison, we add the expected variation of R based on mineral physics if heterogeneity were purely thermal in origin, one estimate (black line) from *Karato* [1993] and the other (gray inverted triangles) from ab initio calculations for $MgSiO_3$ perovskite by *Oganov et al.* [2001].

[64] Measured R in Figure 10a typically increases for $z \gtrsim 400$ km, and is between 1 and 4 for RMS estimates. We note that $R \gtrsim 2.5$ implies a negative correlation between bulk sound and shear wave velocity [e.g., *Masters et al.*, 2000, equation (4)] which is usually interpreted as an indication of compositional heterogeneity. Mean $\langle R \rangle$ values based on δv_{RMS} are, indeed, in general larger than the mineral physics estimates for temperature and pressure effects in Figure 10a, in agreement with findings from direct inversions for R [e.g., *Robertson and Woodhouse*, 1996]. However, lower-end linear regression estimates and RMS $\langle R \rangle$ from sprd6 and SB10L18 (Figure 10b) fall close to the mineral physics values [see, also, *Masters et al.*, 2000] and recent estimates by *Karato and Karki* [2001] are

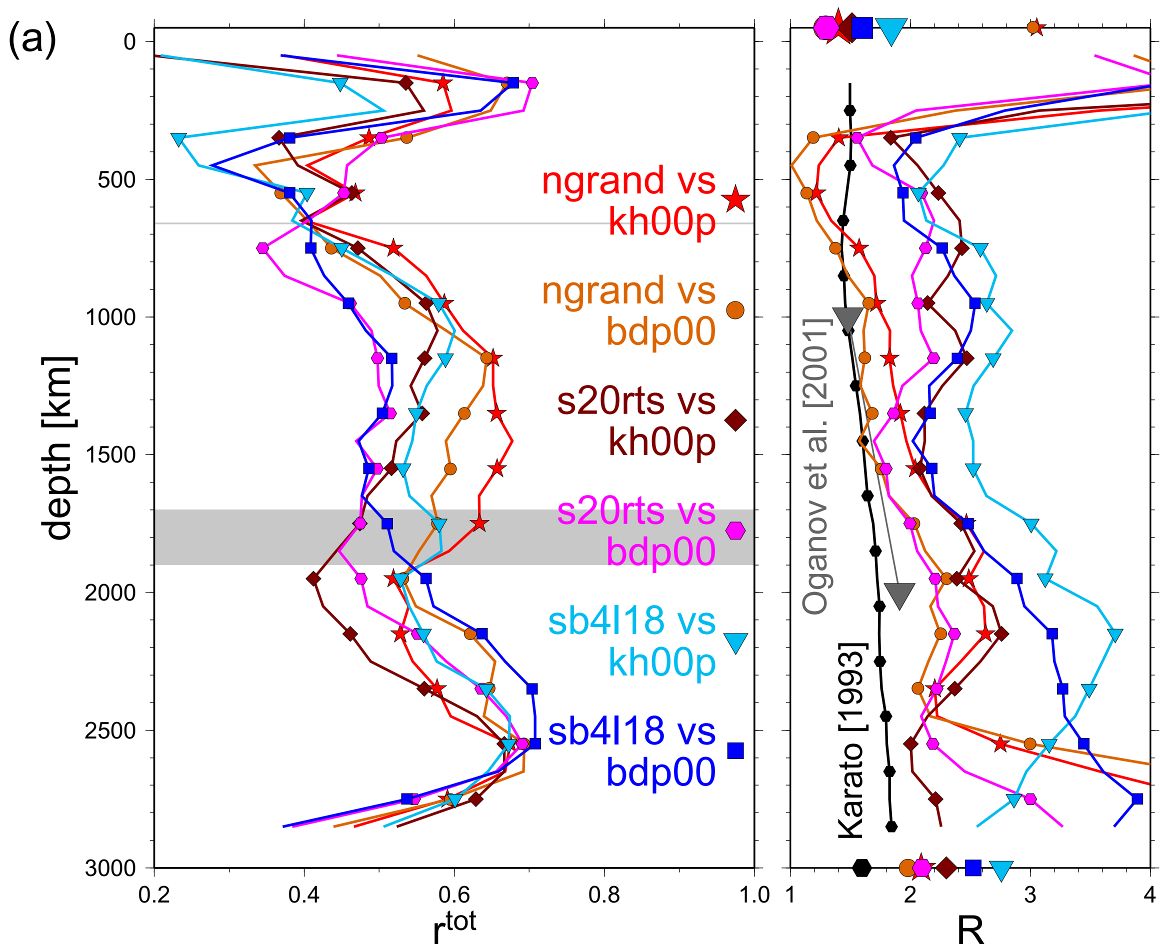

Figure 10. The δv_s-δv_p correlation r^{tot} (left subplots) and $R = \delta v_s/\delta v_p$ (right subplots) for (a) a combination of S and P models and (b) MK12WM13, SB10L18, smean/pmean, and SPRD6. Estimates of r^{tot} are based on $\ell_{max} = 20$ (r_{20}^{tot}, solid) and $\ell_{max} = 8$ (r_8^{tot}, dashed lines in Figure 10b, except for SPRD6 which is always r_6^{tot}) and R is from the RMS ratio (solid lines) and an iterative linear regression (error bars in Figure 10b, lower and higher estimates are for $\Sigma_{\delta v_s} = 2\Sigma_{\delta v_p}$ and $\Sigma_{\delta v_p} = 2\Sigma_{\delta v_s}$, respectively). Symbols on R axis indicate mean $\langle R \rangle$ for $z \geq 400$ km from the RMS ratio (at z = 3000 km) or lower and higher estimates from linear regression (at z = 0, large and small symbols, respectively).

larger than *Karato*'s [1993] R values by ~0.4. Hence the significance of the observed mid-mantle deviations from a homogeneous composition trend remains to be determined.

[65] In synthesis, judging from r and R for δv_s–δv_p, regions of global deviation from the predictions of mineralogy for a chemically homogeneous mantle are likely to be limited to the tectosphere, the transition zone (where data coverage for P is inferior), the CMB region, and, less pronounced and with all the caveats from section 4.1.3, the depth range at ~2000 km.

4.2.4. Geodynamic models

[66] The correlation between two subduction models, stb00d and lrr98d, is shown in Figure 11. They are most consistent in the upper mantle where slab locations are well con-

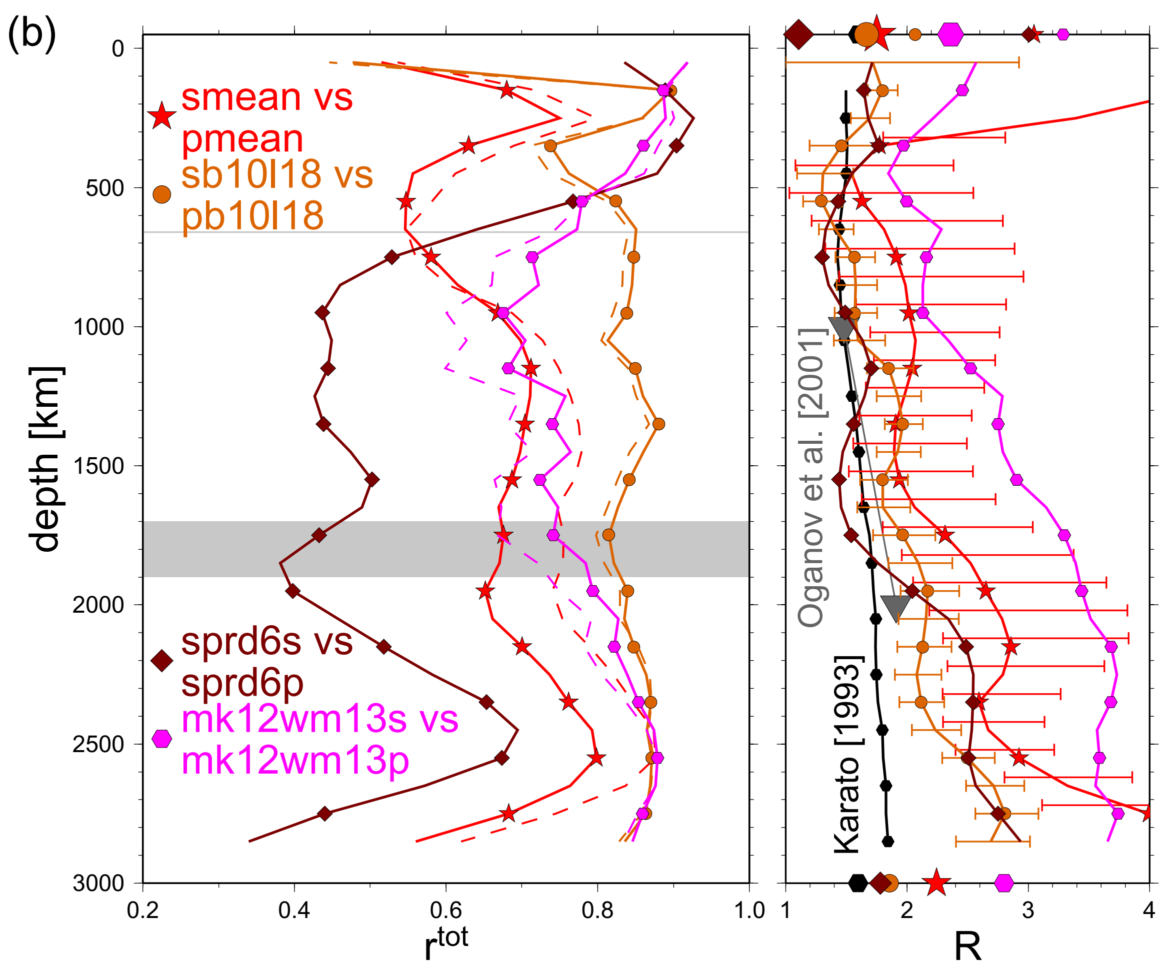

Figure 10. (continued)

strained by seismicity ($\langle r_8 \rangle$ with rum is 0.63 and 0.61 for lrr98d and stb00d, respectively). Moreover, advection is only active in stb00d once slabs sink below 380 km. *Steinberger*'s [2000b] and *Lithgow-Bertelloni and Richards*' [1998] approach should therefore lead to very similar results for shallow structure. Once lateral advection becomes more important with depth, correlation decreases with z up to $\sim$1000 km and stays low for $\ell \gtrsim 5$ throughout the lower mantle. The finding that the geodynamic models do not agree well with each other globally ($\langle r_8 \rangle = 0.44$) implies that differences in methodology and the effect of lateral advection on the narrow slab features affect the global measure r significantly (see section 4.3). This observation can also guide us as to how to judge the correlation of slab and tomography models.

[67] The r^ℓ between geodynamic and tomographic models is in fact high for long wavelengths ($\ell \lesssim 3$) [*Ricard et al.*, 1993; *Lithgow-Bertelloni and Richards*, 1998] throughout the mantle, but r^ℓ is low for higher ℓ. We find that global $\langle r_8 \rangle$ is small on average ($\langle r_8 \rangle \sim 0.3$) and there is no clear depth-dependence of r_8^{tot}, besides that correlation is usually largest below

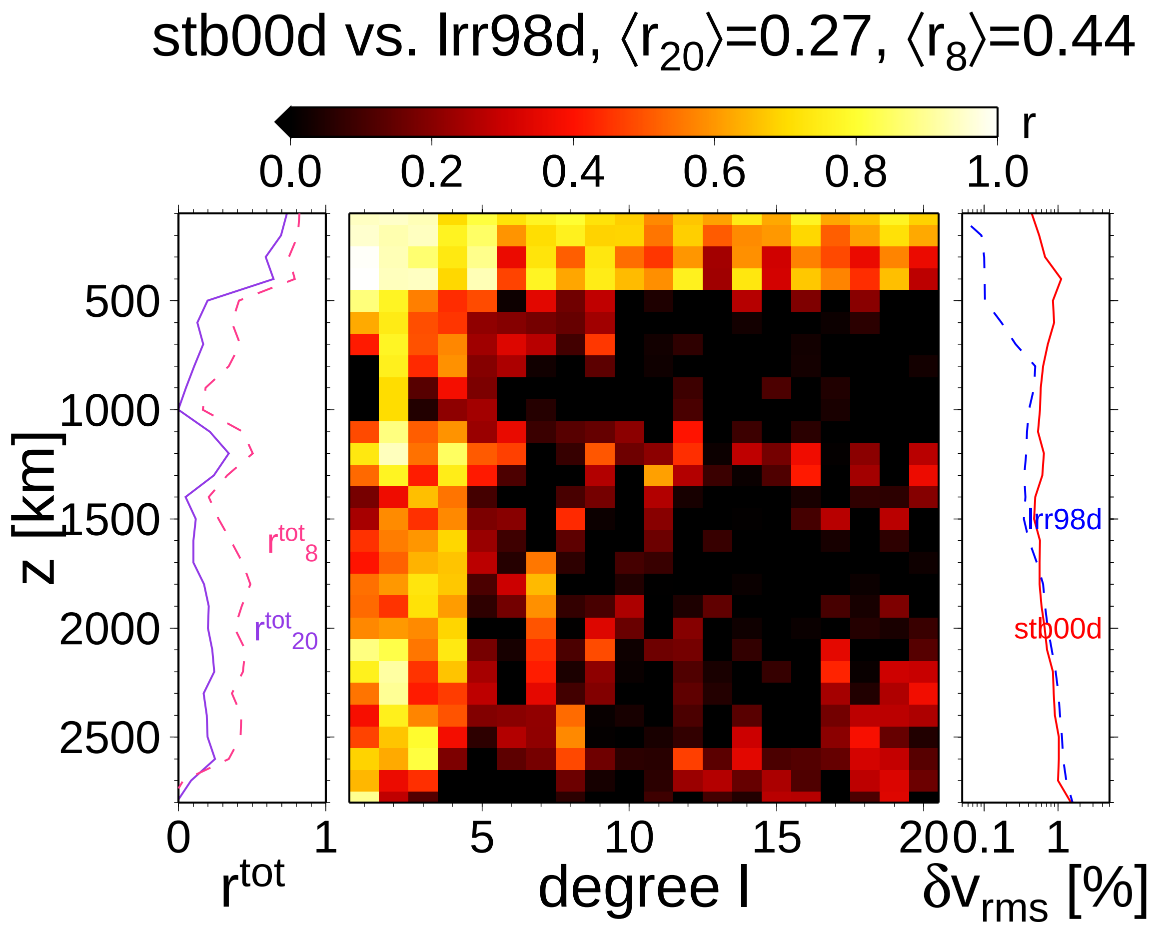

Figure 11. Cross-model correlation for stb00d (solid δv_{RMS}-line) and lrr98d (dashed δv_{RMS}-line). Compare with Figure C6 and see Figure 7 for description.

the transition zone at ~800 km and smallest at $z \sim 1500$ km depth (see the additional online material). The best $\langle r_8 \rangle$-correlation between subduction and tomography models is $\langle r_8 \rangle$ = 0.33 between lrr98d and smean (see Figure 23 and section 4.2.5), but lrr98d and stb00d lead to very similar $\langle r_{20} \rangle$-results ($\langle r_{20} \rangle$ = 0.18 and $\langle r_{20} \rangle$ = 0.21 with smean, respectively).

4.2.5. Summary of average cross-model correlations

[68] We summarize our findings in Figure 12 which shows the total depth-averaged correlations $\langle r_8 \rangle$ and the total cross-model correlations at 600 km, 1400 km, and 2750 km, for a selection of *P*, *S*, and geodynamic models. (For $\langle r_{20} \rangle$, see the additional online material.) In general, agreement between tomography is poor at $z \sim 600$ km (where *S* models correlate fairly well with subduction models) and increases with larger depths. We find that our models smean and pmean correlate better ($\langle r_8 \rangle$ = 0.71) with each other than any other δv_s-δv_p combination in Figure 12a and achieve the highest $\langle r_8 \rangle$ with slab models lrr98d or stb00d. For the *S* models that were not used for the construction of smean (see appendix B), the discontinuity models s20a and s362d1 are

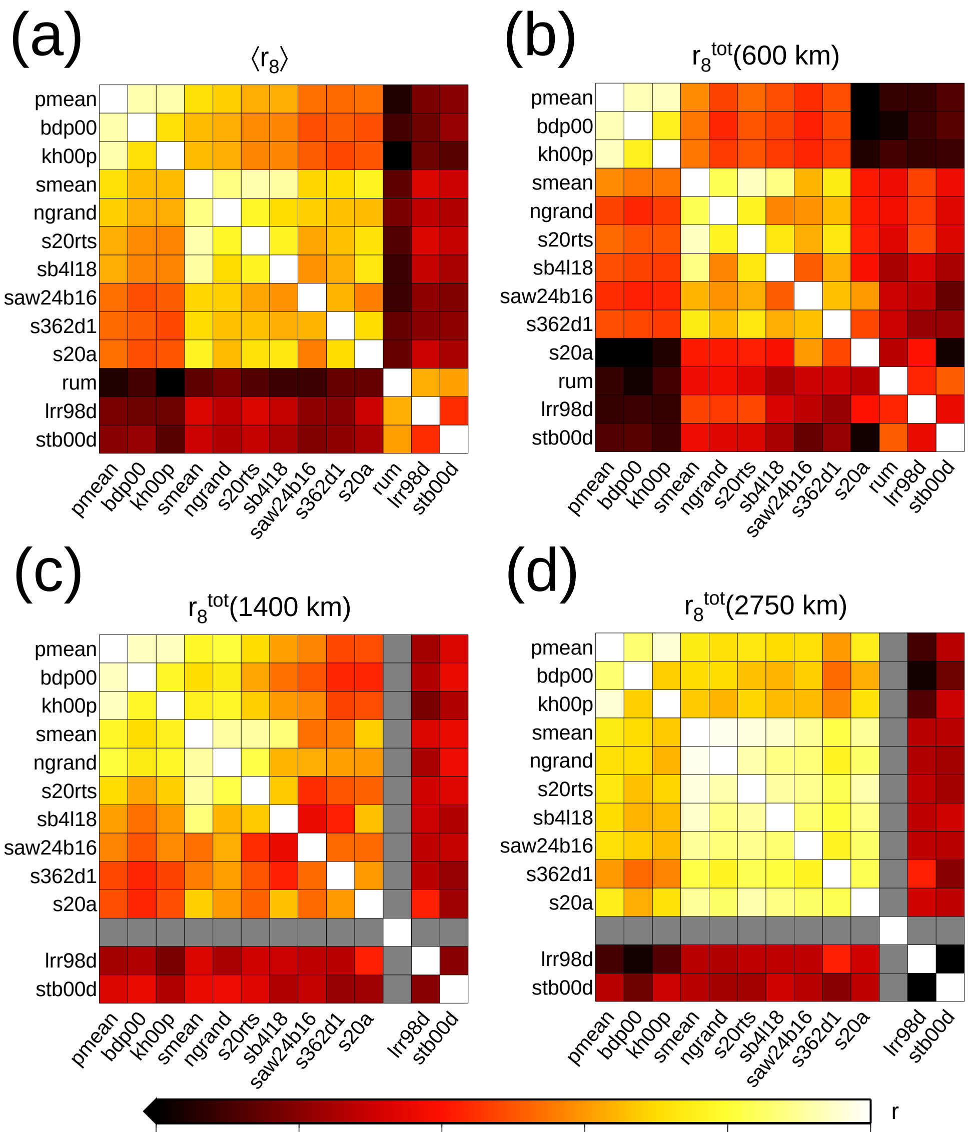

Figure 12. Average cross-model correlation up to (a) $\ell_{\max} = 8$ ($\langle r_8 \rangle$, as well as (b) r_8^{tot} at z = 600 km, (c) z = 1400 km, and (d) z = 2750 km.

found to be more similar to smean than saw24b16 which is δv_{sh} only. We cannot identify particular depth ranges where anisotropy in S wave propagation might cause deviations. However, we note that correlation between smean and saw24b16 has a local minimum in the lower mantle (see the additional online material) where *Mégnin and Romanowicz* [1999] argue that their approach has led to improved resolution over other S models.

[69] From Figure 12 we can also see that subduction models correlate better with S than with P models. On average, lrr98d is about as similar to tomographic models (mean $\langle r_8 \rangle / \langle r_{20} \rangle$ from Figure 12 is 0.24/0.13) as stb00d (mean

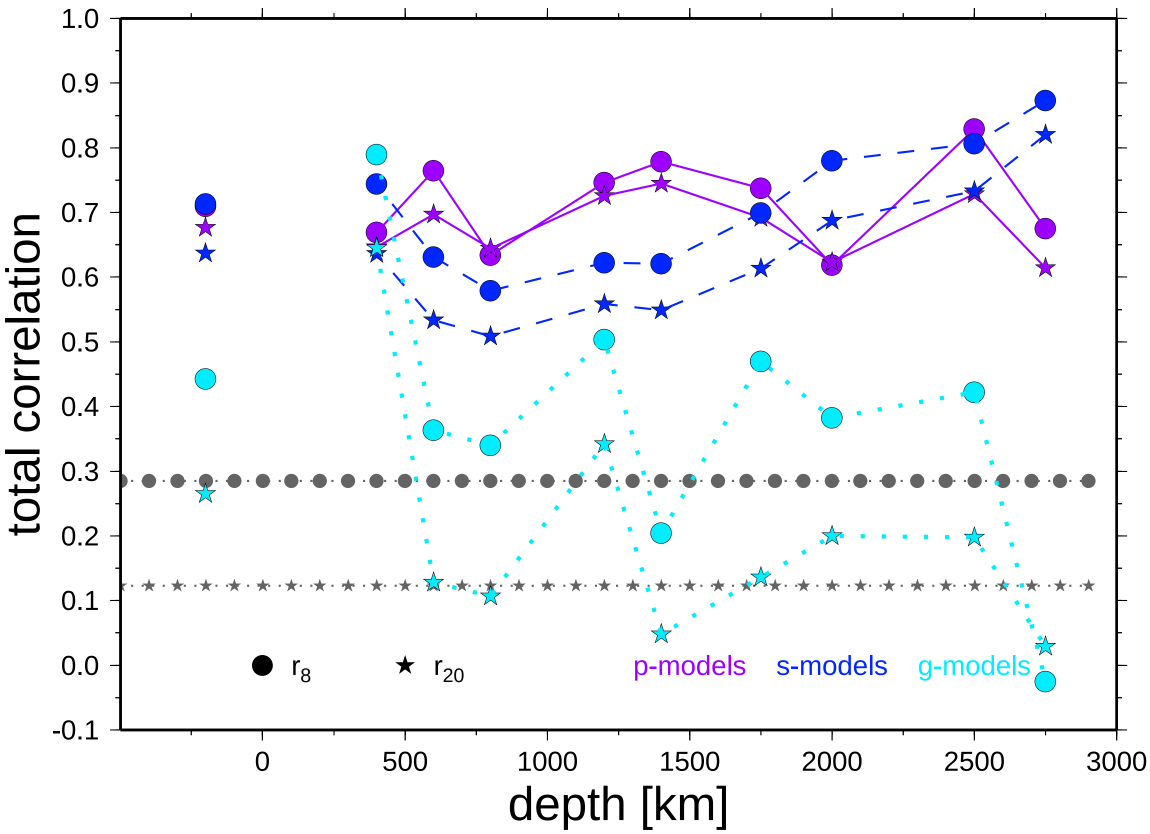

Figure 13. Cross-model correlations for *P* models (solid lines), *S* models (dashed lines), and geodynamic models ("g," dotted lines). Symbols at negative depth indicate $\langle r \rangle$, and line-connected symbols are r^{tot}. Circles and stars denote r_8^{tot} and r_{20}^{tot}, respectively, and horizontal lines show the 99% significance levels (see appendix A).

$\langle r_8 \rangle / \langle r_{20} \rangle$ is 0.23/0.16), even though stb00d is a more sophisticated model in terms of the treatment of mantle flow. We will discuss these findings further in section 4.3.

[70] In a final step toward cross-model similarity synthesis, Figure 13 explores how similar *P* (bdp00 and kh00p), *S* (s362d1, s20a, sb4l18, saw24b16, s20rts, and ngrand), and geodynamic models (stb00d and lrr98d) are on average. The highest correlations are generally associated with the longer wavelength component (*S* models in particular) and, for tomography, larger depths. Subduction models become progressively uncorrelated with increasing *z*.

4.3. Comparison of Tomography and Geodynamic Models

[71] We have seen that the geodynamic models stb00d and lrr98d do not correlate well globally with tomography for $\ell \gtrsim 5$. We now argue that this does not imply that there is no slab signal in the mantle but that our understanding of flow modeling has to be improved.

4.3.1. Subduction versus fast anomalies only

[72] Slabs in the mantle will be colder than their surroundings and thus show up as fast anomalies only. Therefore we set to zero all

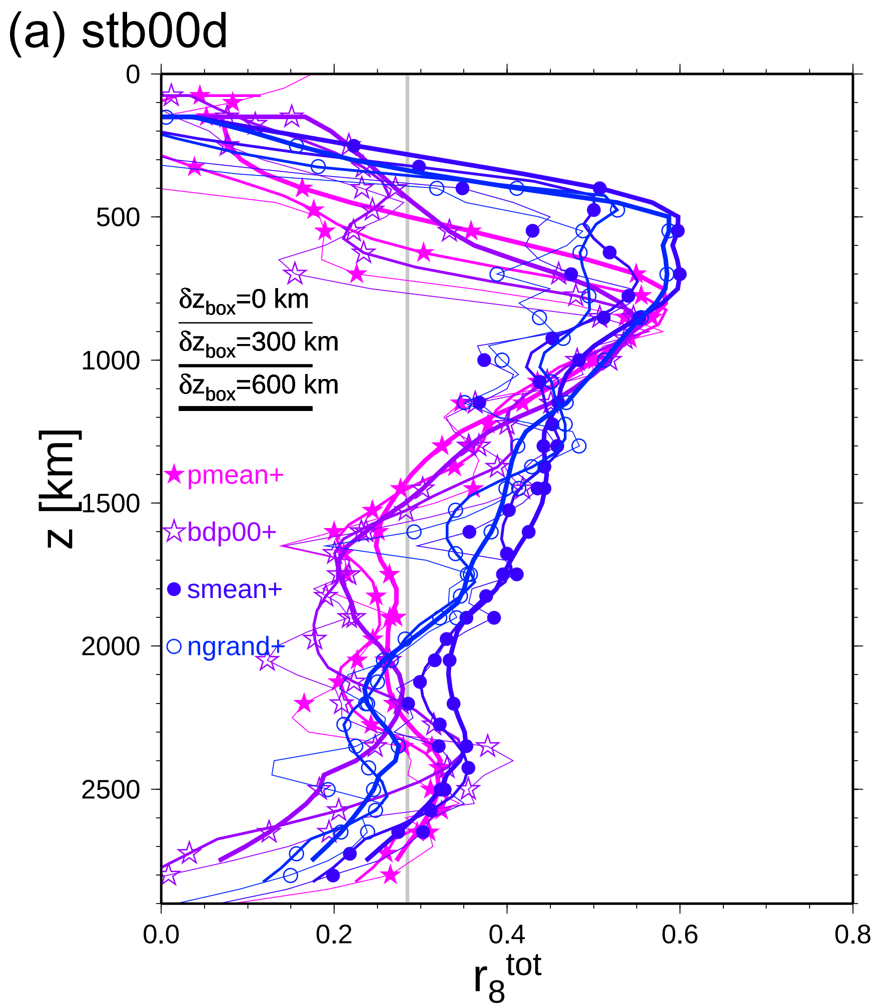

Figure 14. The r_8^{tot} of (a) stb00d and (b) lrr98d with *P* and *S* models for radial boxcar averaging. Line thickness indicates δz_{box}; the vertical gray line denotes the 99% confidence level.

slow anomalies present in tomographic models, reexpand the models, thus "clipped," and recompute their correlation with the geodynamical models. This procedure leads to some increase in the correlation between lrr98d, stb00d, rum, and tomography models, particularly in the upper and middle mantle. However, the depth-averaged correlation is still poor ($\langle r_8 \rangle \leq 0.4$). We thus infer that the low global correlation between tomography and subduction models cannot be explained as an effect of the lack of independent hot upwellings in subduction models. An alternative explanation is that our knowledge of mantle viscosity and of the velocity at which slabs sink is still incomplete. We will now analyze this possibility with additional calculations.

[73] We smooth the depth-dependence of stb00d and lrr98d by taking, for each expansion, a sliding boxcar average with depth extent

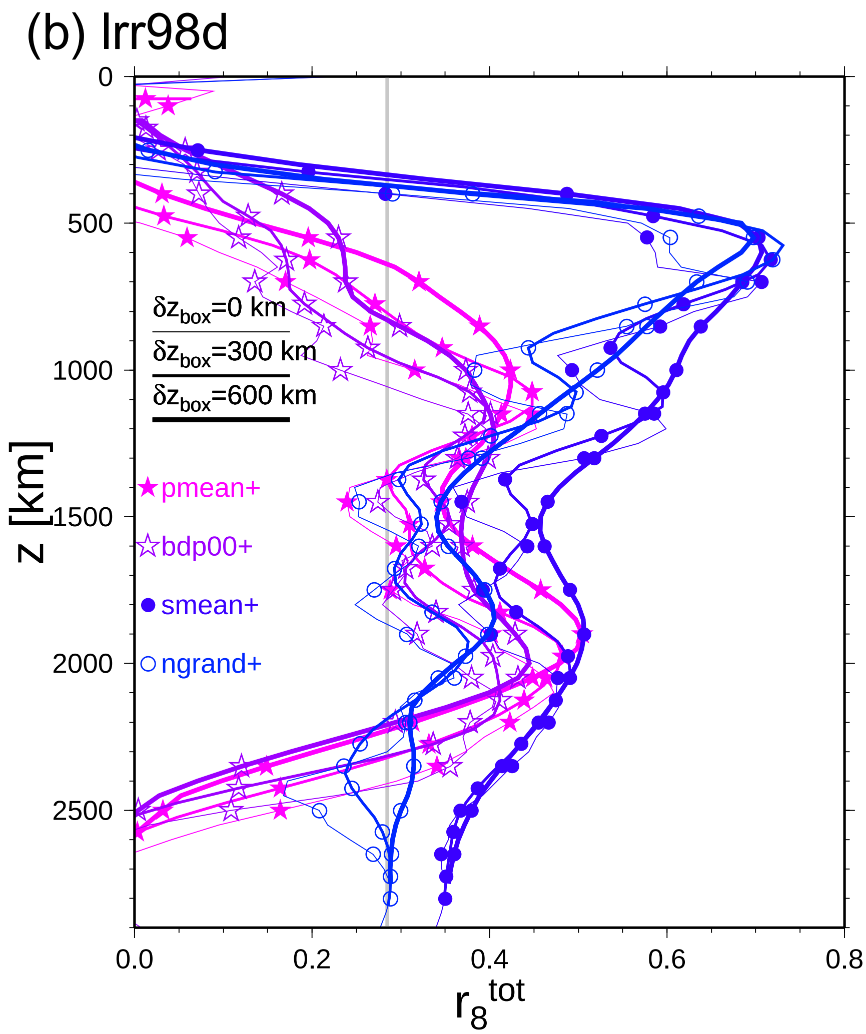

Figure 14. (continued)

δz_{box} up to 600 km (mean of [z - δz_{box}/2; z + δz_{box}/2]) and then find, again, the r_8^{tot} correlation between stb00d (Figure 14a) or lrr98d (Figure 14b) and several clipped ($\delta v > 0$) tomography models. The results, summarized in Figure 14, indicate that correlation becomes higher with increasing δz_{box}. Our radial smoothing filter therefore limits problems associated with the short radial correlation length Δz of subduction models. We find that correlations are higher with S models, and the behavior of r_8^{tot} as a function of depth is different depending on the model (stb00d or lrr98d, see section 4.3.2). In general, r_8^{tot} is negative in the shallow mantle ($z \lesssim 200$ km) owing to the tectosphere and continent or ocean differences imaged by tomography but not included in the subduction models. The r_8^{tot} then increases to its maximum in the middle mantle ($z \sim 750$ km) where slabs might be more easily detected by tomography since an increase in viscosity at 660 km could lead to a broadening of the subduction signal in

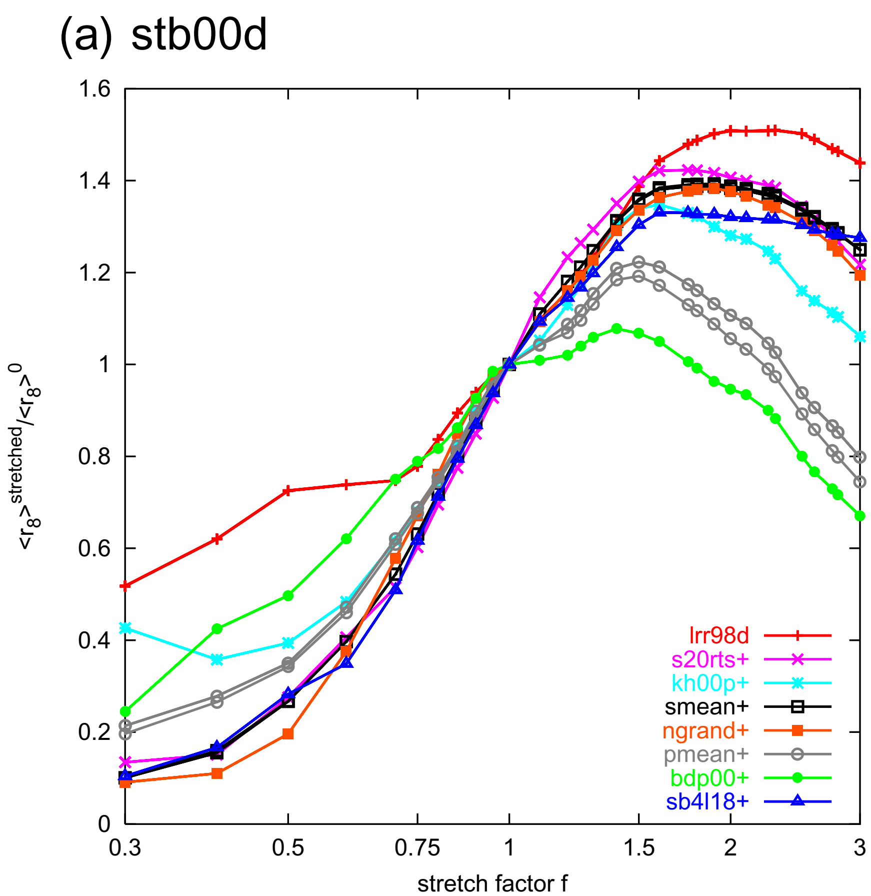

Figure 15. New cross-model $\langle r_8 \rangle$ over original $\langle r_8 \rangle$ if model (a) stb00d or (b) lrr98d are stretched by f.

the lower mantle. Correlation then decreases toward the CMB.

4.3.2. Effect of slablet sinking speed

[74] We simulate the effect that a wrong estimate of the sinking velocity of slablets would have on subduction models: neglecting lateral motion, upper/lower mantle differences, and upwellings, this can be done by "stretching" the models by a factor f, i.e., mapping the depth interval $[z_a, z_b]$ onto $[fz_a, fz_b]$ (Figure 15). For stb00d, $\langle r_8 \rangle$ with clipped tomography can be improved by up to 43% (Figure 15a) with the best $f_{\text{opt}} \sim 1.75$, corresponding to a higher sinking speed. As Figure C6 shows, lrr98d and the modified stb00d are more similar ($\langle r_8 \rangle = 0.66$) in this case, too. However, individual $\langle r_8 \rangle$ correlations of the stretched stb00d with tomography ($\langle r_8 \rangle \leq 0.42$) are still not much better than for lrr98d, for which we find $f_{\text{opt}} \sim 0.75$ with a smaller relative increase of $\langle r_8 \rangle$ of $\leq 20\%$ ($\langle r_8 \rangle \leq 0.38$), most pronounced for P models (Figure 15b). This implies that *Lithgow-Bertelloni and Richards*' [1998] optimization with respect to the sinking velocity was basically successful; *Steinberger*'s [2000b] more realistic subduction calculation with fewer free parameters and lateral advection

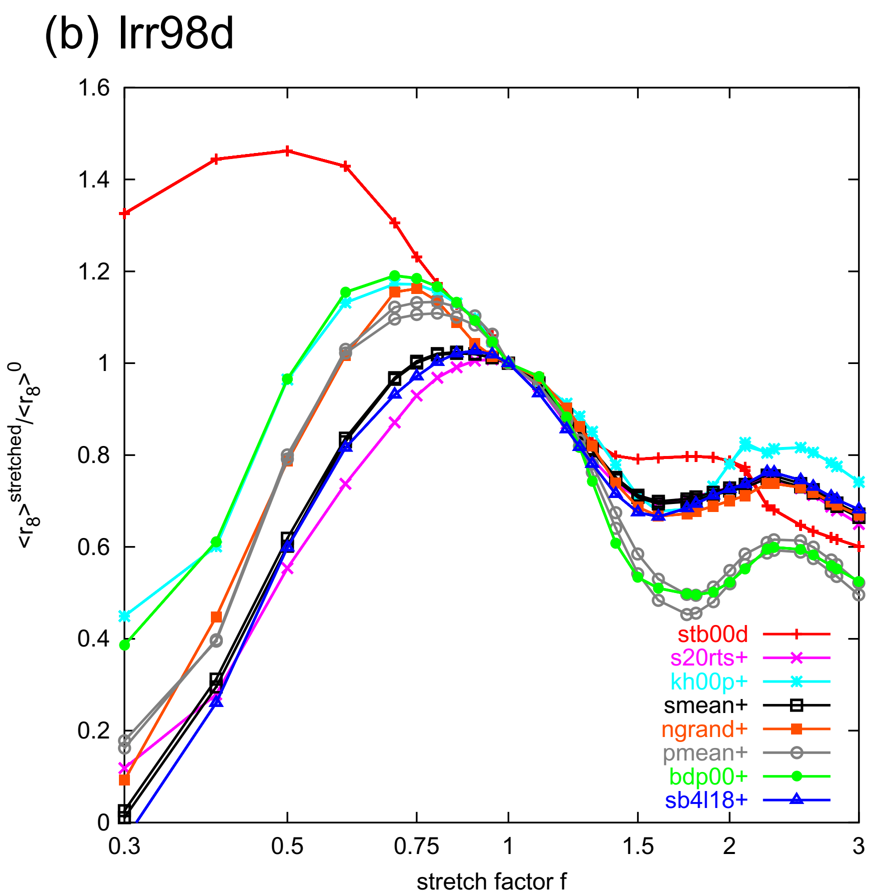

Figure 15. (continued)

did not produce a better model when global correlation with tomography is used as a measure.

[75] In synthesis, we find that geodynamic models show some resemblance to tomographic models on a global scale. The correspondence is best at ~800 km depth but not as good as between tomographic models. The reason for this could be that the subduction process is not yet modeled correctly and the lateral and depth offsets that might result from slab interaction with 660 km [e.g., *Zhong and Gurnis*, 1995; *Christensen*, 1996] could explain some of the weak correlation at intermediate ℓ. Especially transient slab flattening or segmentation (already invoked to account for changes in spectral characteristics) will degrade the global correlation as the comparison between the two, fairly similar, subduction models shows.

[76] Inaccuracies in the advection process are, of course, not the only possible explanation for the poor global agreement between subduction models and tomography. One question that needs to be considered is the precision to which we can infer past plate motions and how subsequent modifications in the reconstructions will map themselves into the large scale density

field. However, other effects such as (possibly local) compositional heterogeneity might also be important.

4.3.3. Midmantle slabs

[77] Figures 16 and 17, including clipped tomographic and geodynamic maps above (550 km) and below 660 km (850 km), substantiate our finding that subduction models are most similar to tomographic ones at $z \sim 800$ km. Some of the seismically active trenches (e.g., Japan, Kurile, Solomon, and Peru-Chile) are clearly present at $z = 550$ km in all models (Figure 16). (We show average fields from 500 to 600 km.) However, only ngrand includes a distinct image of the Tonga and Indonesia slabs; strong fast anomalies underneath North America appear only in the P models. Also, older slab material might have accumulated in the Mediterranean [e.g., *Wortel and Spakman*, 2000]: we can find such a signal most clearly in kh00p.

[78] Figure 16 also shows that at 550 km depth, all the P models include other, probably not slab-related, fast anomalies beneath the cratonic regions of Canada, Africa, Eurasia, and Australia. Since the tectosphere is believed to terminate at $z < 550$ km and S models (well constrained in the upper mantle, see section 2.2) are not anomalously fast in the same regions, we suggest that these $\delta v_p > 0$ features are partly due to a fictitious effect ("smearing") of the nonuniform coverage achieved by P body wave data. At 850 km depth (Figure 17), all models are remarkably consistent under the Americas, Indonesia, eastern Phillipines, and Tonga, with a robust slab signal below 660 km. With the exception of the mantle below Africa, s362d1 is the only model to include strong fast anomalies that are clearly not subduction-related.

[79] Figure 18 shows the correlation, at 550 and 850 km, between clipped tomography models and, alternatively, rum (Figure 18a), stb00d (Figure 18b), and lrr98d (Figure 18c). The correlation values that we find are statistically significant at the 99% level for most models at 850 km and at least for S models at 550 km depth. Again, we attribute the low correlation obtained from P models in the upper mantle to the nonuniform ray coverage inherent to seismic observations of P velocity (see sections 4.2.5 and 4.3.1). This is an important consideration if P models are to be interpreted geodynamically. In most cases, the highest values of tomography versus geodynamic correlation are found at $\sim$850 km (see 4.3.2), confirming that most fast seismic anomalies found in the middle-mantle are slab-related.

4.3.4. Slow velocity anomalies

[80] Identifying convective features in tomographic models is more difficult for slow than for fast wave speed anomalies. While slabs are of great importance for mantle convection [e.g., *Davies and Richards*, 1992], we also expect to see some trace of the upwellings be it in the form of large-scale swells or narrow plumes. It is not clear, however, if global tomography is able to image the latter features at this stage [e.g., *Ritsema et al.*, 1999].

[81] We clip tomographic models as above, now eliminating all positive velocity anomalies, and then compare the resulting "slow-anomaly-only" models with δ-function expansions of hot spot distributions from *Steinberger* [2000a] and 3SMAC [*Nataf and Ricard*, 1996]. The resulting values of r_8^{tot} are given in appendix C7 (Figure C7). As noted by *Ray and Anderson* [1994], there is no clear correlation between surface hot spot locations and tomographically mapped anomalies (the correlation is statistically significant only near the surface and at $z \sim$

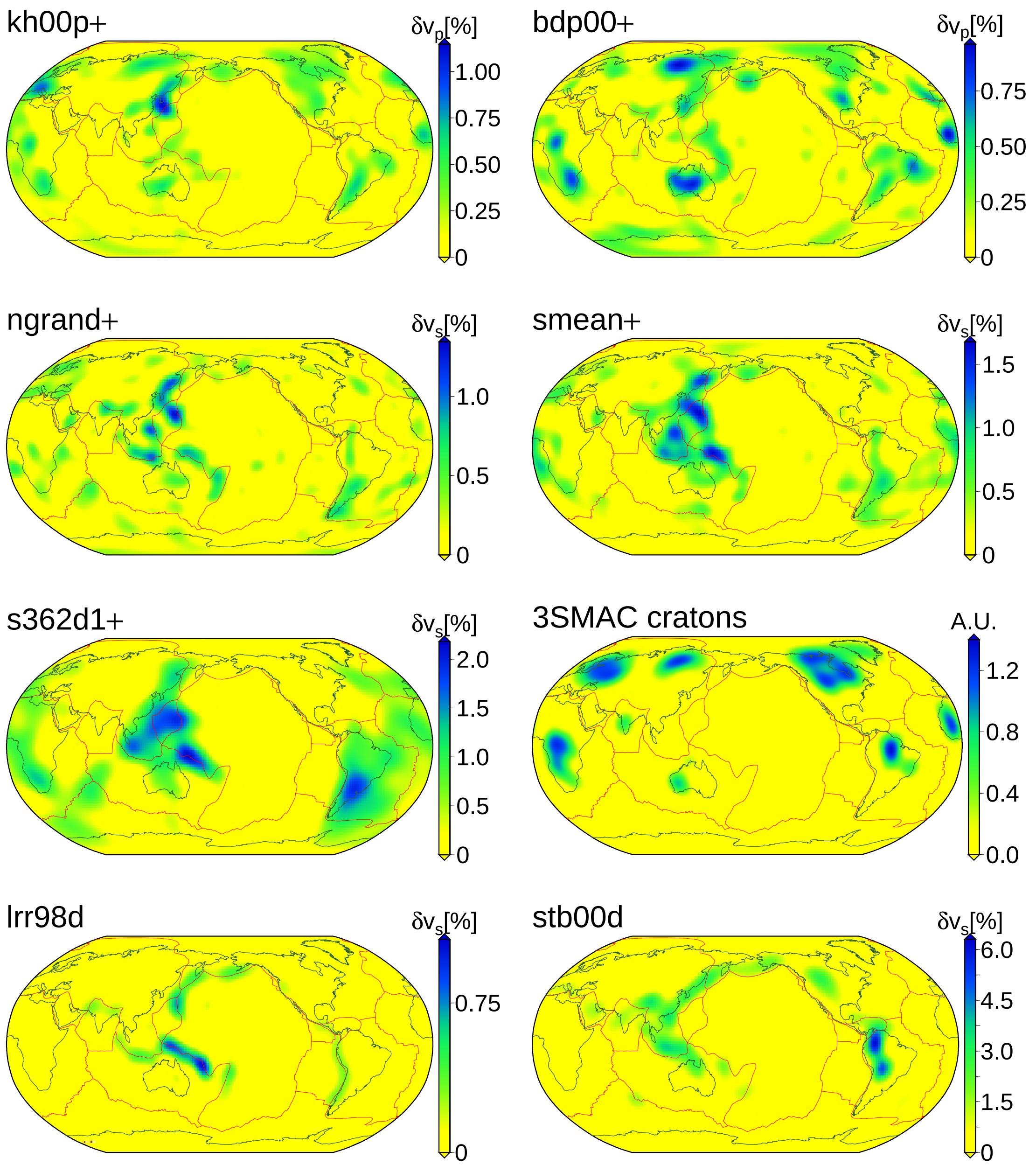

Figure 16. Comparison of tomographic models (positive δv only, "+"), old cratons from 3SMAC [*Nataf and Ricard*, 1996], and geodynamic models with $\ell_{max} = 20$ at $z = 550$ km (average from 500 km to 600 km depth, $\delta z_{box} = 100$ km, Robinson projection). Red plate boundaries are from NUVEL-1 [*DeMets et al.*, 1990].

1500 km). However, this does not imply that hot spots are not plume-related since plume conduits are likely to be deflected during their ascent [e.g., *Steinberger*, 2000a] and larger scale downwellings might affect the plume source locations in the deep mantle [e.g., *Richards et al.*, 1988; *Steinberger and O'Connell*, 1998].

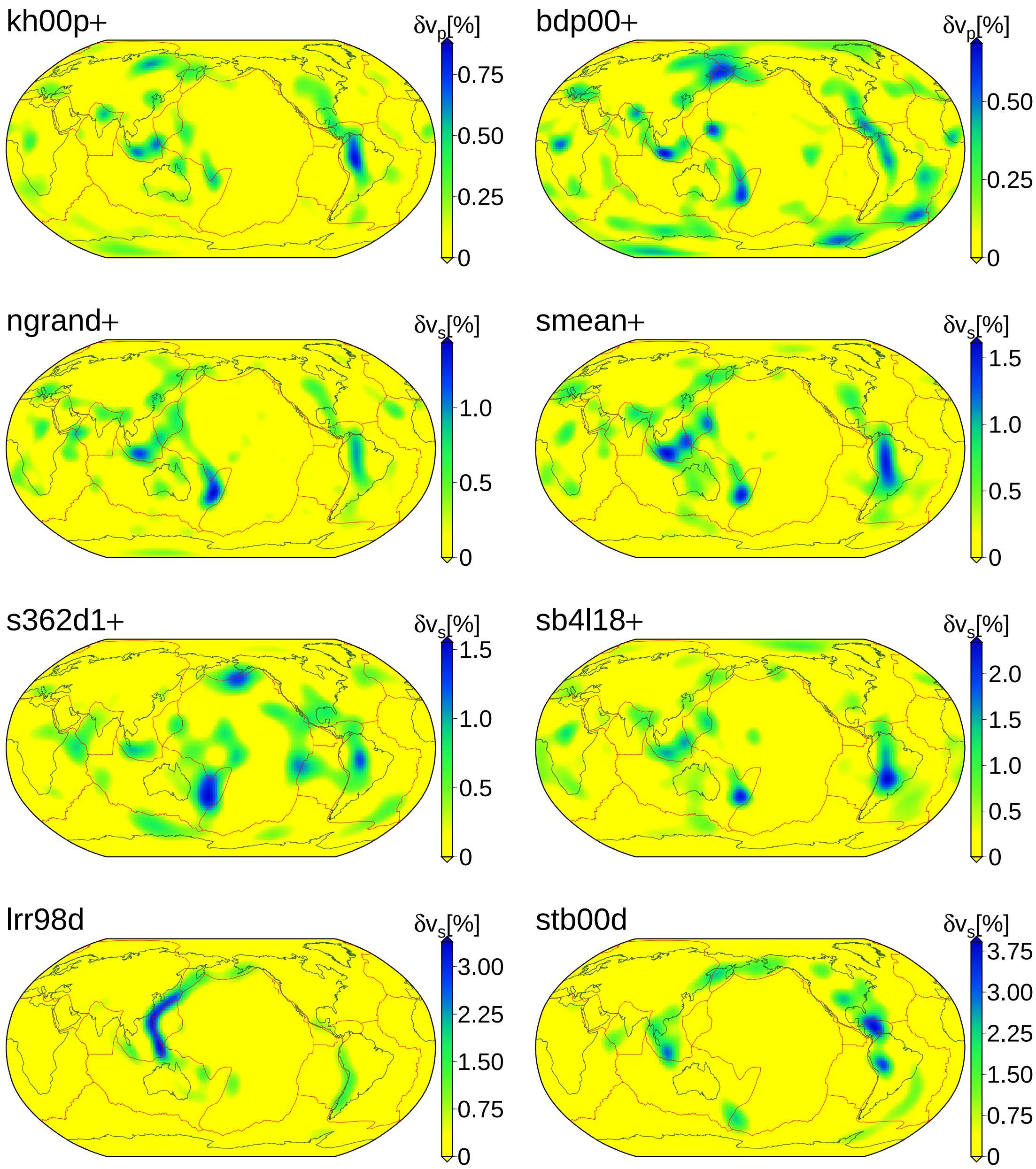

Figure 17. Comparison of positive δv only tomography and geodynamic models, z = 850 km (average from 800 km to 900 km). 3SMAC cratons were replaced with sb4l18+.

[82] Certain slow anomalies that are not ridge-related appear systematically in all tomographic models at z = 300 km (see Figure C8): around the Afar region and Iceland (possibly related to plumes), in the southwestern Pacific (possibly related to the superswell), and in the central Pacific region. The latter anomaly is of complex structure, widespread, and

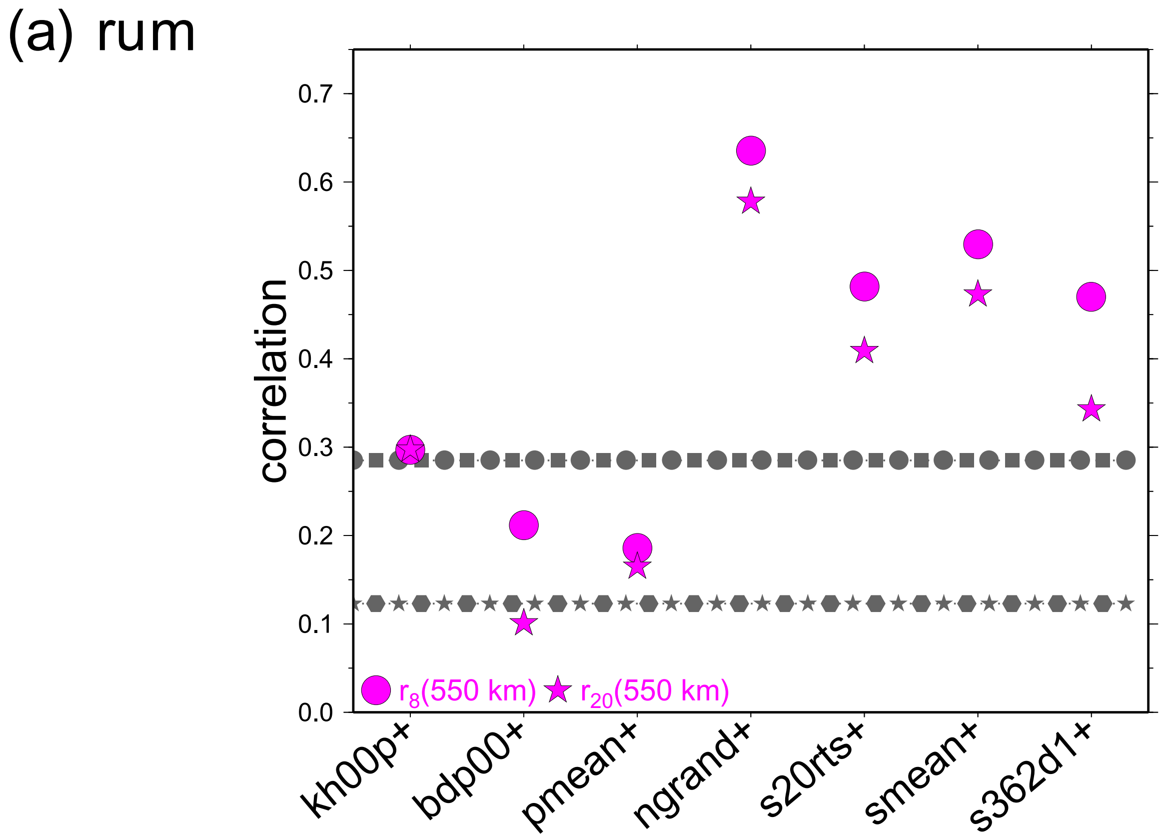

Figure 18. Correlation of fast anomaly only tomography and (a) rum, (b) stb00d, and (c) lrr98d slab models. Symbols denote r_8^{tot} and r_{20}^{tot} for layer correlations at z = 550 km and z = 850 km with δz_{box} = 100 km. Horizontal lines are 99% confidence levels.

lies in a region where seismic observations are affected by strong radial anisotropy [*Ekström and Dziewonski*, 1998]. At z = 1500 km (Figure C9), all models are dominated by two large anomalies centered on southwest Africa and the central Pacific (thus characterized by a strong $\ell = 2$ component); of these, at least the African one stretches down to the CMB in more than one model [e.g., *Dziewonski*, 1984]. At 2500 km depth (Figure C10), we find that the African anomaly is accompanied by one underneath the Antarctic plate at 60°E, 60°S. The Pacific part of the $\ell = 2$ pattern can also be separated into three subanomalies, the westernmost lying underneath the Nazca plate (see, also, Figure C1).

5. Conclusions

[83] The spectra of seismic models of the Earth's mantle are predominantly of long spatial wavelength [e.g., *Su and Dziewonski*, 1992]. We have found that the long-wavelength components of most tomographic models published within the last decade are systematically well correlated with each other, indicating a substantial agreement between different techniques. As a general

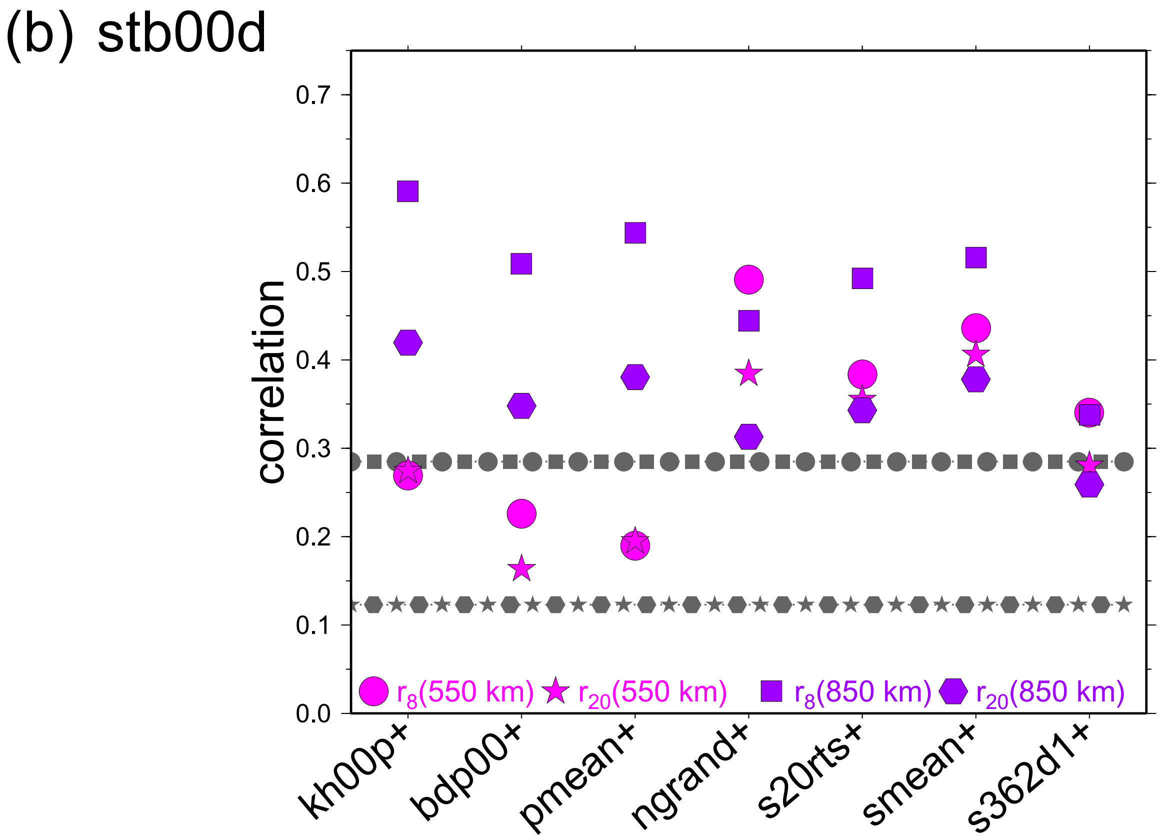

Figure 18. (continued)

rule, correlation is highest in the lowermost mantle (see, e.g., Figures 12 and 13), where the coverage of teleseismic travel-time data is most uniform [e.g., *van der Hilst et al.*, 1997]. Although most models are described with a fine lateral parameterization (at least up to spherical harmonic degree $\ell = 20$, or equivalent), correlation is always lower for shorter spatial wavelengths, especially for *S* models (Figures 7–9). This suggests that, so far, attempts to image the smaller (~1000 km) scale structure of the mantle have not been equally successful. The correlation between models of the same type is significantly higher than when *P* and *S* models are compared with each other. This discrepancy can partly be explained in terms of different sensitivities of the *P* and *S* data sets to lateral structure at different depths. Correlation between δv_s and δv_p anomalies is lowest in the upper mantle and at the CMB (Figures 9 and 10), where a common thermal origin might not be sufficient to explain the imaged heterogeneities but compositional anomalies could be invoked.

[84] We found some evidence for a change of the spectral character of heterogeneity below 660 km and local minima in the radial correlation function at ~700 km for *S* and *P* models (Figures 4–6) but failed to detect strong layering or global discontinuities at other depths in the mantle. However, as the 660 km discontinuity model s362d1 and cross-model discrepancies at ~2000 km show, interesting depth ranges in the mantle coincide with those depths

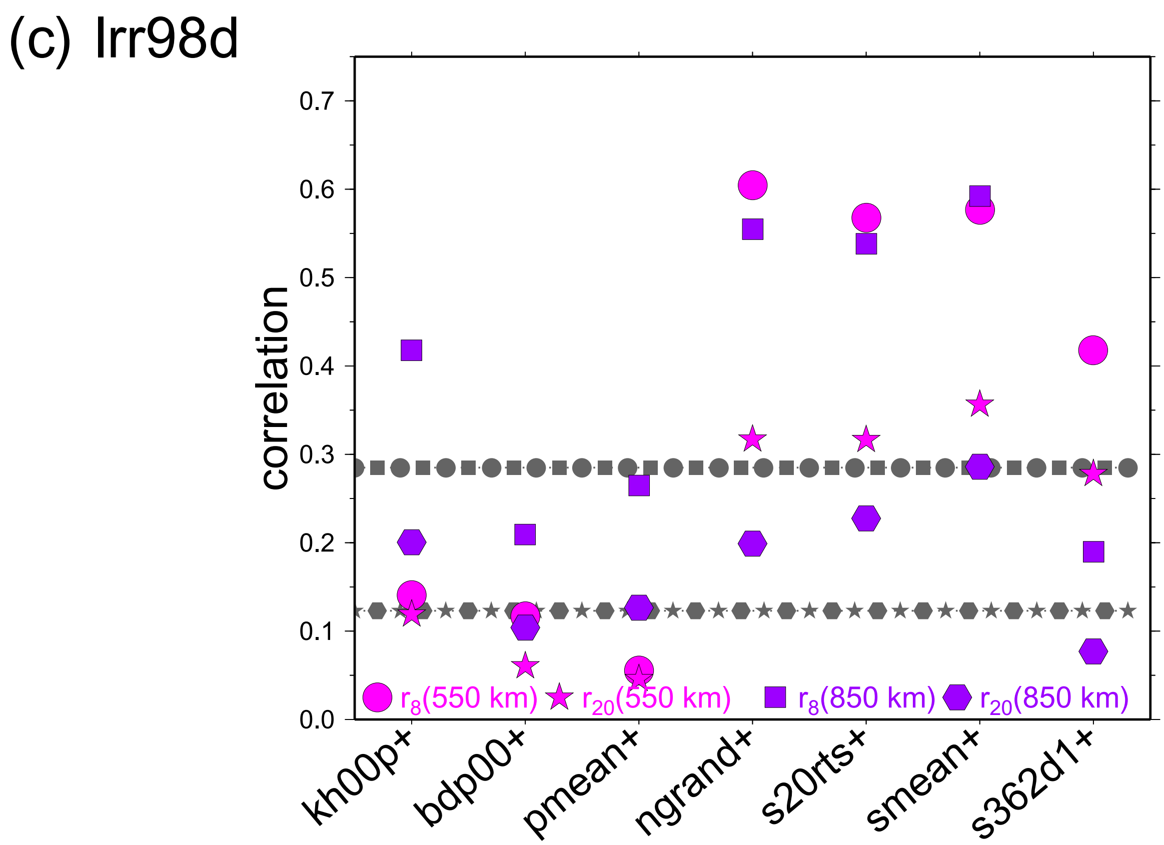

Figure 18. (continued)

where tomographic model consistency is still limited.

[85] Tomography does not correlate well globally with models based upon geodynamic reconstructions of mantle flow for $\ell \gtrsim 5$; seismic observations and subduction history models do not yet produce identical images. We have, however, found that fast anomalies are imaged consistently in the midmantle where we would expect slabs in the absence of a long-term barrier to flow at 660 km (Figures 14 and 17). This substantiates previous studies [*van der Hilst et al.*, 1997; *Čížková et al.*, 1998; *Bunge et al.*, 1998], and slab penetration is found to be a common phenomenon (Figure 18). As discussed, it can be expected that future flow models will do a better job in predicting slab locations and current discrepancies should lead to a better understanding of the nature of the subduction process.

[86] Our results are consistent with an emerging whole mantle convection paradigm in which the phase transition, with a probable viscosity increase, at 660 km can lead to transient slab flattening and flow reorganization but, in the long term, subduction maintains a high mass flux between the upper and lower mantle.

Appendix A. Statistical Significance of Linear Correlation

[87] Assuming a binormal distribution for the deviations from a linear trend, we can apply Student's t test [*Press et al.*, 1993, p. 637] to

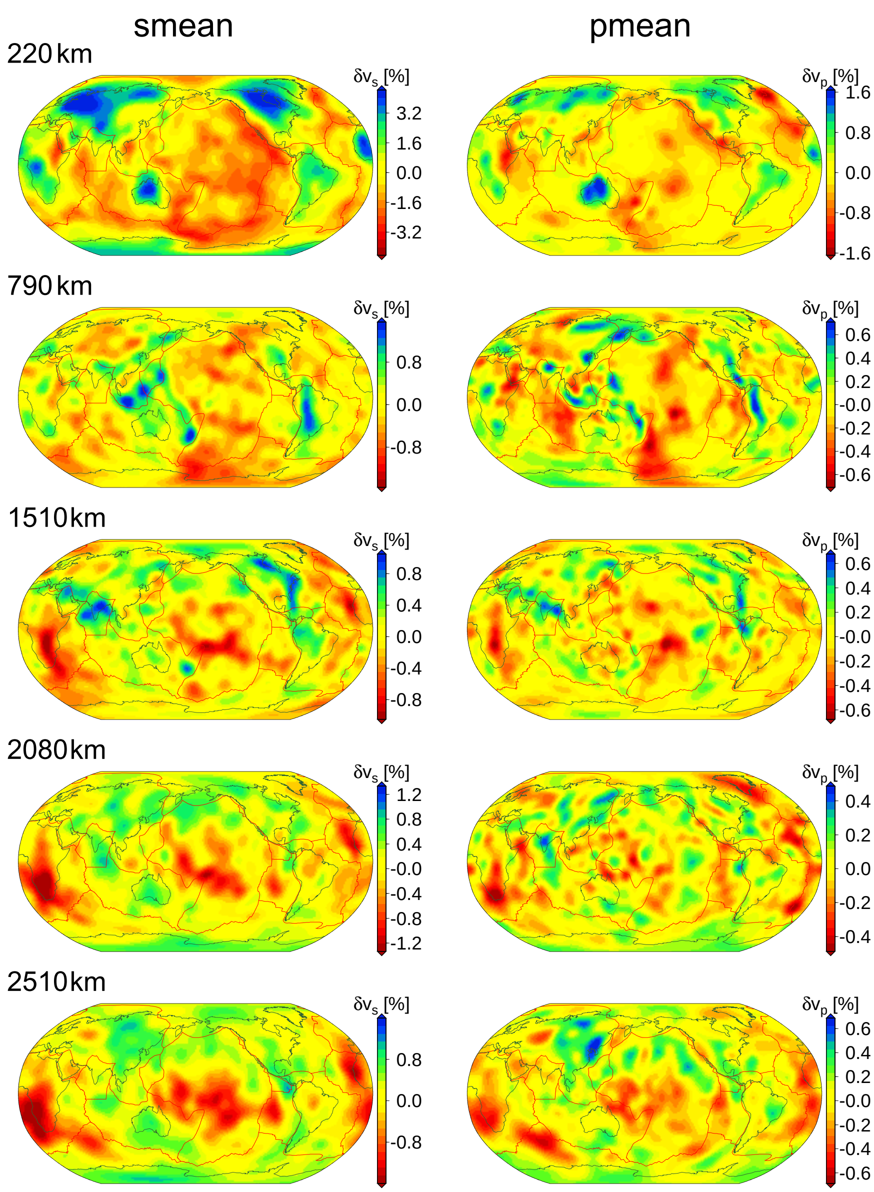

Figure C1. (left) The smean (δv_s) and (right) pmean (δv_p) at the indicated depths, $\ell_{\max} = 31$.

evaluate the likelihood, p, that a correlation r between two sets of coefficients is caused by chance. The number of degrees of freedom is $(\ell_{\max} + 1)^2 - 3$; for $\ell_{\max} = 20$ and $\ell_{\max} = 8$, the 99% significance levels ($p = 0.01$) for r are then given by 0.123 and 0.286, respectively. Most of the r values we find are therefore "significant" at the 99%-level, although care should be taken when interpreting such statements [e.g., *Ray and Anderson*, 1994].

Appendix B. Construction of Mean Models

[88] To create an ad hoc reference against which we can compare individual models, we con-

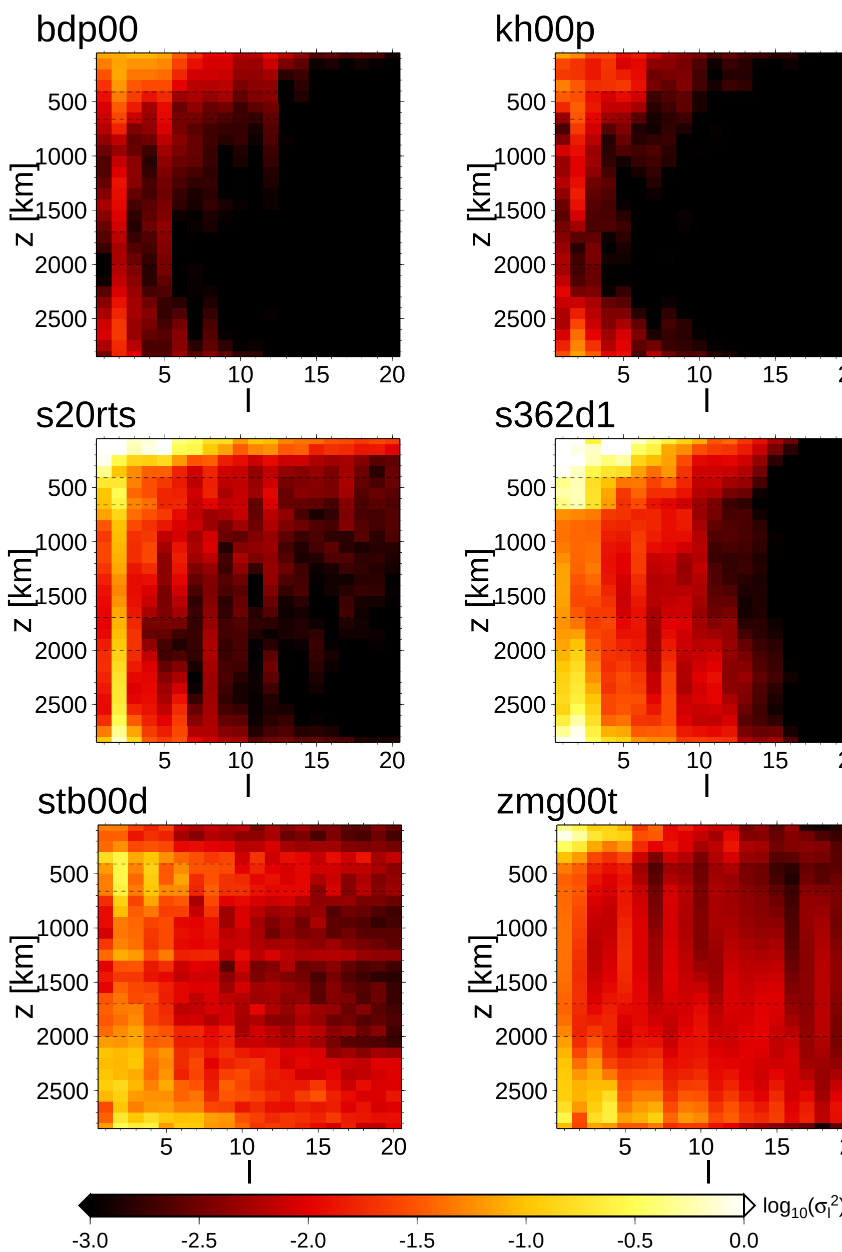

Figure C2. Absolute power per degree and unit area on a logarithmic scale, $\log_{10}(\sigma_\ell^2)$, for *P*, *S*, and geodynamic models (compare Figure 1 and additional online material).

struct "stacked" *P* and *S* wave tomography models. Models smean and pmean have been calculated by a weighted average of well-correlated *S* models with similar input data (ngrand, s20rts, and sb4l18) and the newer *P* wave models (bdp00 and kh00p), respectively. We first determine depth-averaged δv_{RMS} for each input model and then scale the models

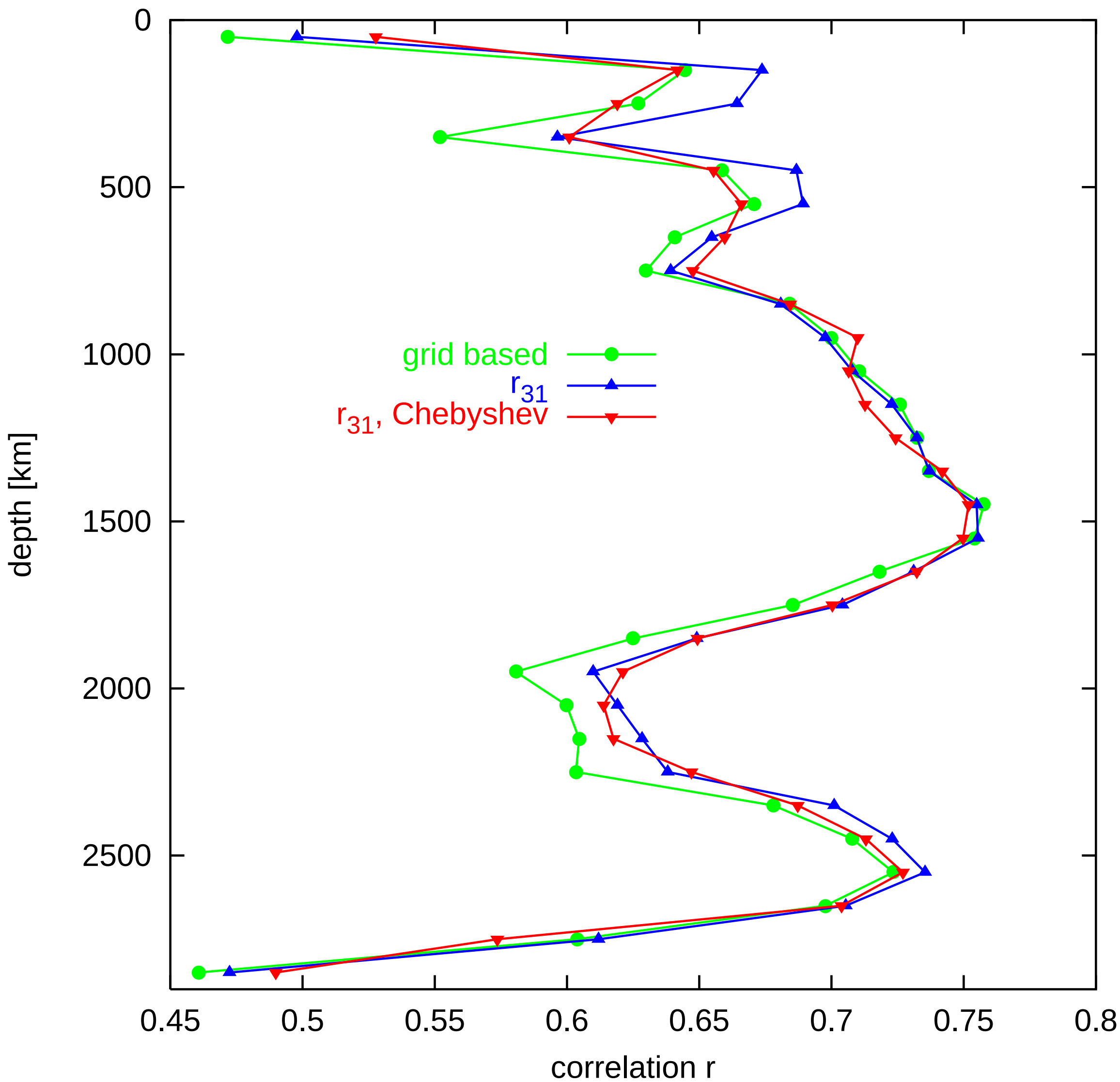

Figure C3. Comparison of total correlations between bdp00 and kh00p based on grids (circles) with spherical harmonics, r_{31} (after equation (9), triangles), and spherical harmonics based on a $k_{\max}$ = 20 Chebyshev reparameterization (inverted triangles).

such that they would lead to a mean model with a depth-averaged δv_{RMS} that corresponds to the mean δv_{RMS} of all input models. This procedure maintains the depth dependence of δv_{RMS} for each model but evens out total heterogeneity amplitude differences between models. (We have experimented with additional, ℓ-dependent average correlation weighted models, results were not much different.) The spatial expansion of the resulting mean models is shown at selected depths in Figure C1 (for the spectral and δv_{RMS} character, see Figures 2 and 3 and the additional online material).

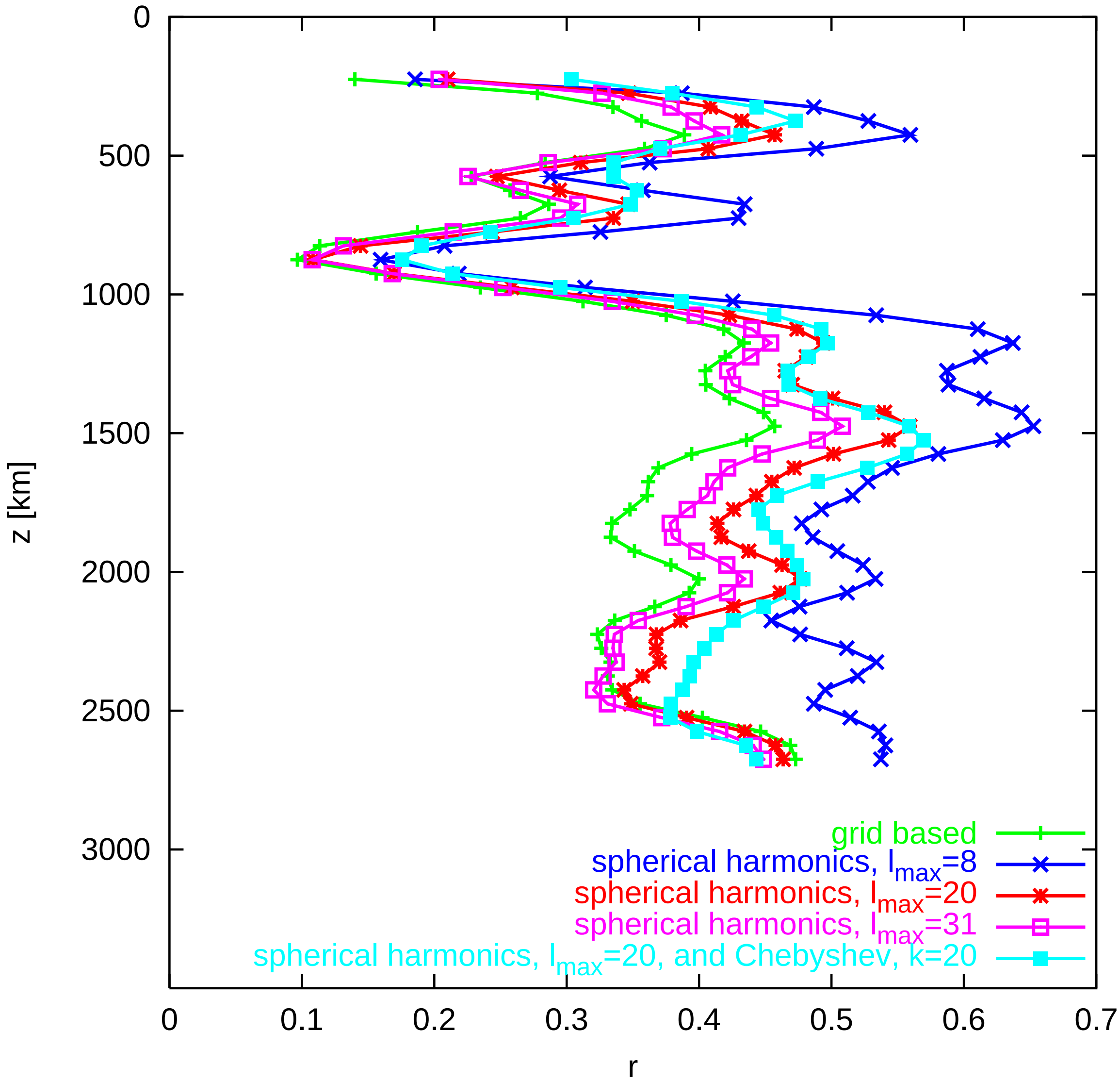

Figure C4. Radial correlation function estimates ($r(z - \Delta z, z + \Delta z)$ at Δz = 200 km) for different parameterizations of kh00p: grid based, spherical harmonics laterally for ℓ_{max} = 8, ℓ_{max} = 20 (identical to results in Figure 4b), and ℓ_{max} = 31, as well as ℓ_{max} = 20 spherical harmonics and Chebyshev polynomials radially.

Appendix C. Additional Material

C1. Mean Model Features

[89] Figure C1 shows maps of our mean tomographic models smean and pmean at selected midlayer depths, confirming that the structures that were discussed in sections 4.3.3 and 4.3.4 are robust features of tomography.

C2. Absolute Power Spectra

[90] Figure C2 shows absolute power, σ_ℓ^2, to be compared with the normalized spectral power, $\hat{\sigma}_\ell^2$, shown in Figure 1.

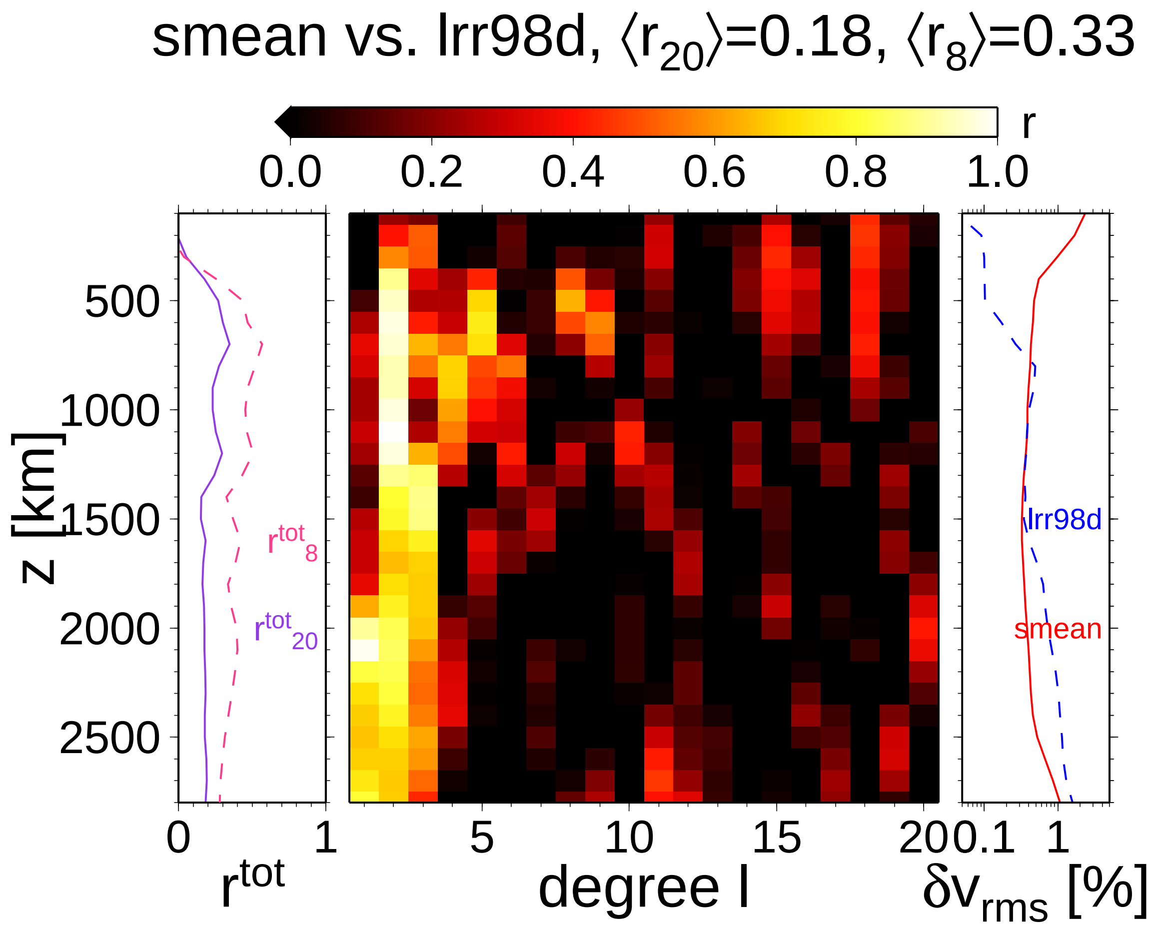

Figure C5. Cross-model correlation for lrr98d (solid δv_{RMS}-line) and smean (dashed δv_{RMS}-line); see Figure 7 for description.

C3. Comparison of Grid and Spherical Harmonic Correlation

[91] Figure C3 shows a comparison of grid [*Press et al.*, 1993, p. 636] and spherical harmonics based estimates of total correlation between bdp00 and kh00p as a function of depth. The area-weighted, discrete data estimate is based on an expansion of the $\ell_{\max}$ = 31 representation of both fields on 1.4° × 1.4° blocks, and the spherical harmonics estimate is r_{31}, after (9). Both methods yield similar results in general, and we find no systematic deviations with depth. We have also included a r_{31}-correlation estimate that is based on a $k_{\max}$ = 20 radial Chebyshev reparameterization; features are similar but the curve is smoother, as expected.

C4. Alternative Radial Correlation Estimates for kh00p

[92] Figure C4 shows the radial correlation function estimate r at Δz = 200 km for different parameterizations of kh00p. We observe that radial features of our $\ell_{\max}$ = 20 spherical harmonics based estimate as in Figure 4b are very similar to what we would

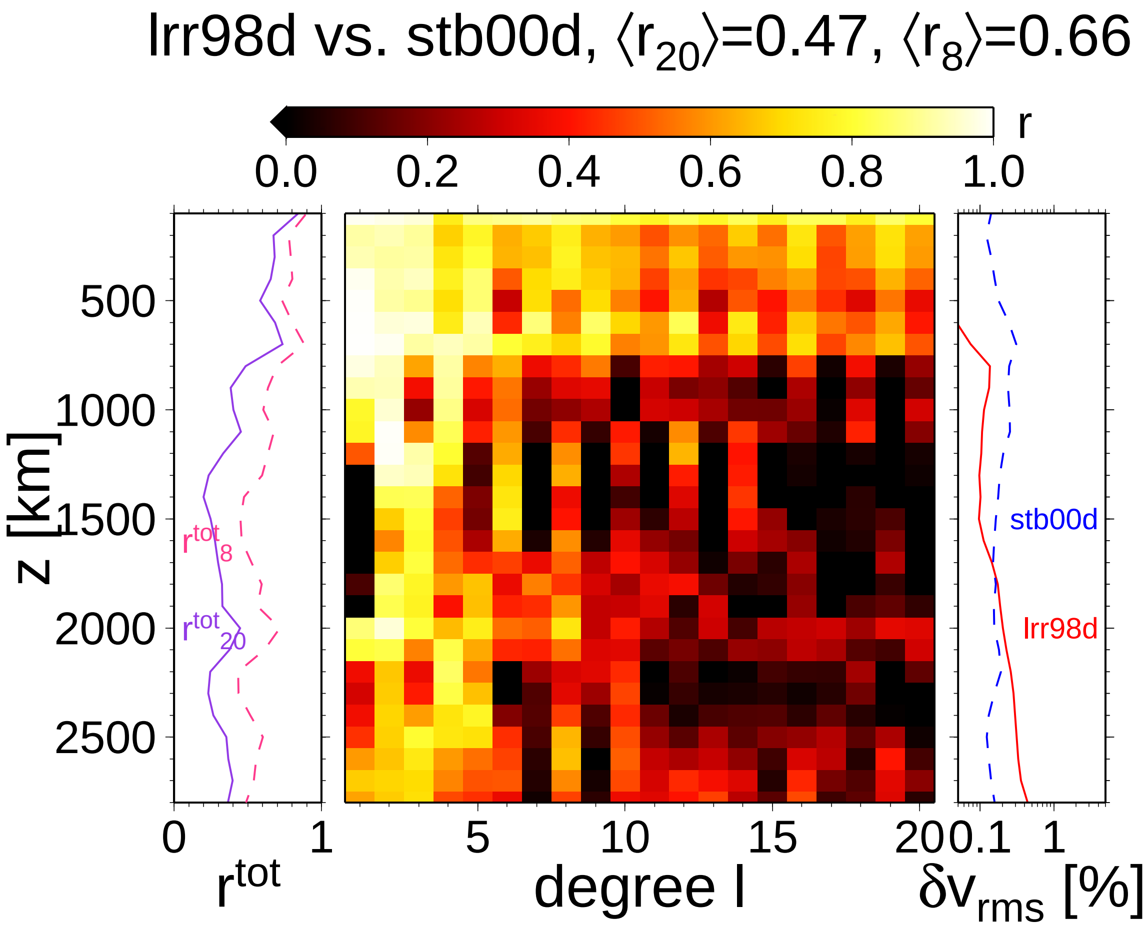

Figure C6. Cross-model correlation for lrr98d (solid δv_{RMS}-line) and f_{opt} = 1.75 stretched stb00d (see section 4.3.2, dashed δv_{RMS}-line). Compare Figure 11, and see Figure 7 for description.

obtain using original grid data (absolute numbers for r differ, however). The comparison of $\ell_{\max}$ = 8 and $\ell_{\max}$ = 31 estimates shows that small-scale structure in r is found across all wavelengths. The Chebyshev radial parameterization introduces some smoothing but is otherwise able to recover the major features of the original model.

C5. Correlation Between lrr98d and smean

[93] Figure 5 shows the cross-model correlation for the best $\langle r_8 \rangle$ pair of subduction and tomography models, lrr98d and smean. However, intermediate wavelength correlation with smean is slightly better for stb00d ($\langle r_{20} \rangle$ = 0.21) than for lrr98d ($\langle r_{20} \rangle$ = 0.18). The depth dependence of r_8^{tot} and r_{20}^{tot} in Figure C5 is similar to that shown in Figure 14 and shows a midmantle maximum.

C6. Comparison Between lrr98d and Stretched stb00d

[94] Figure C6 shows the cross-model correlation for lrr98d and the f_{opt} = 1.75, stretched

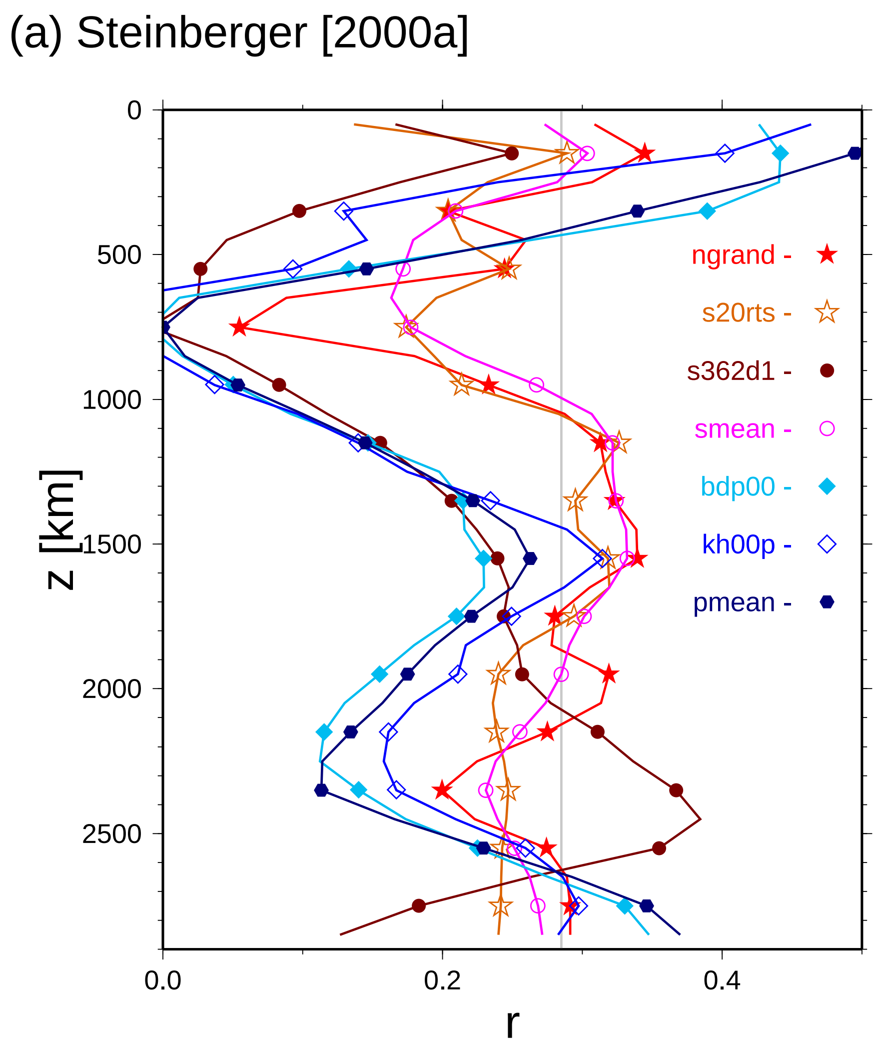

Figure C7. The r_8^{tot} correlation between negative δv only tomography (appended "−") and hot spot function based on (a) *Steinberger* [2000a] and (b) 3SMAC. Gray lines indicate 99% confidence levels. Compare with Figures C8 through C10.

version of stb00d which was discussed in section 4.3.2 as a simplified way to study modified slablet sinking speeds (compare Figure 11). Note that r^ℓ is consistently higher for even than for odd ℓ, especially below 700 km. The even degrees, related to the circum-Pacific subduction, are prominent in the power spectra of stb00d and lrr98d (see Figures 1, C2, and the additional online material) and appear to be best constrained at depth.

C7. Comparison of Slow Anomalies With Hot Spot Locations

[95] To complement our correlation study for fast anomalies, we have expanded the hot spot

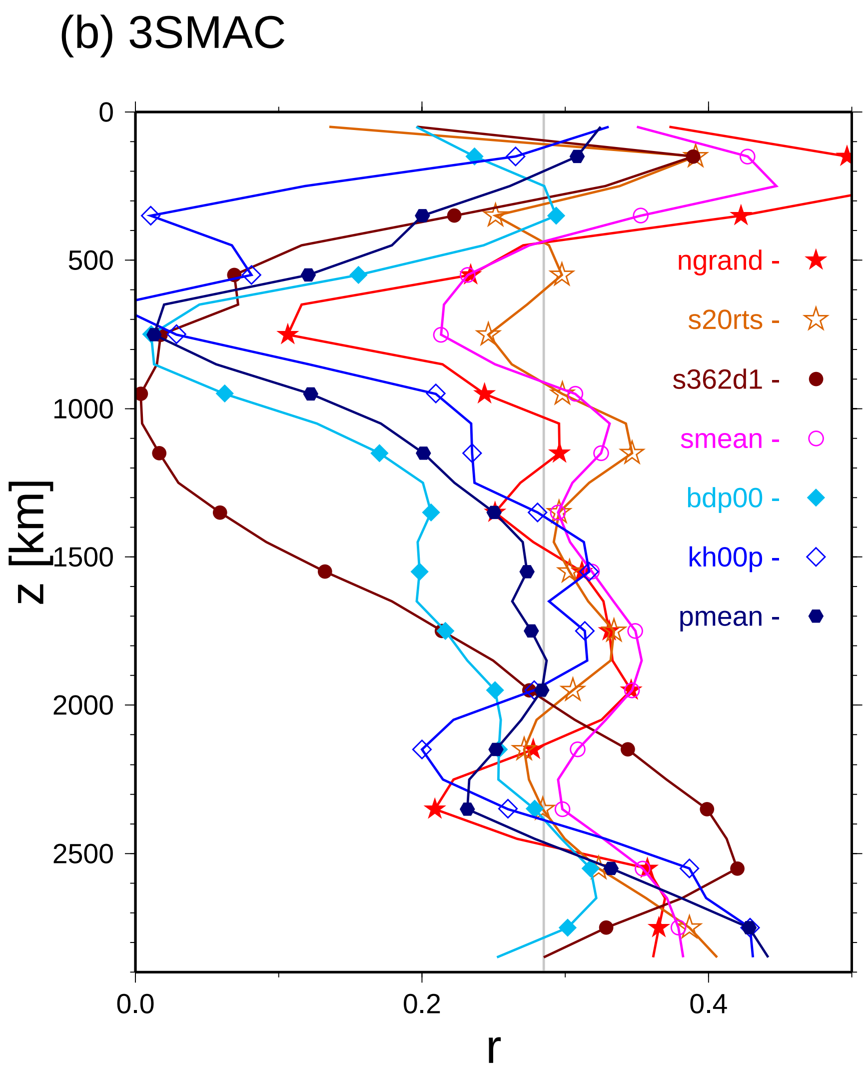

Figure C7. (continued)

lists of *Steinberger* [2000a] and 3SMAC [*Nataf and Ricard*, 1996] as negative δ-functions (damped with a $\cos^2$-taper for $\ell > 0.75\ell_{\max}$) and compared them to slow δv only tomography (r should be positive if hot spots are in $\delta v < 0$ regions). Figure C7 shows that we find only a weak correlation between surface observations of hot spots and slow anomalies that might be connected to rising plumes, consistent with earlier results [e.g., *Ray and Anderson*, 1994]. The correlation is best near the surface, at ∼1500 km, and at the CMB, the depths at which Figures C8 through C10 show the spatial expansions of the fields.

Acknowledgments

[96] We are indebted to all authors of the seismic and geodynamic models for sharing their results and insights. We also want to thank our reviewers Rob van der Hilst

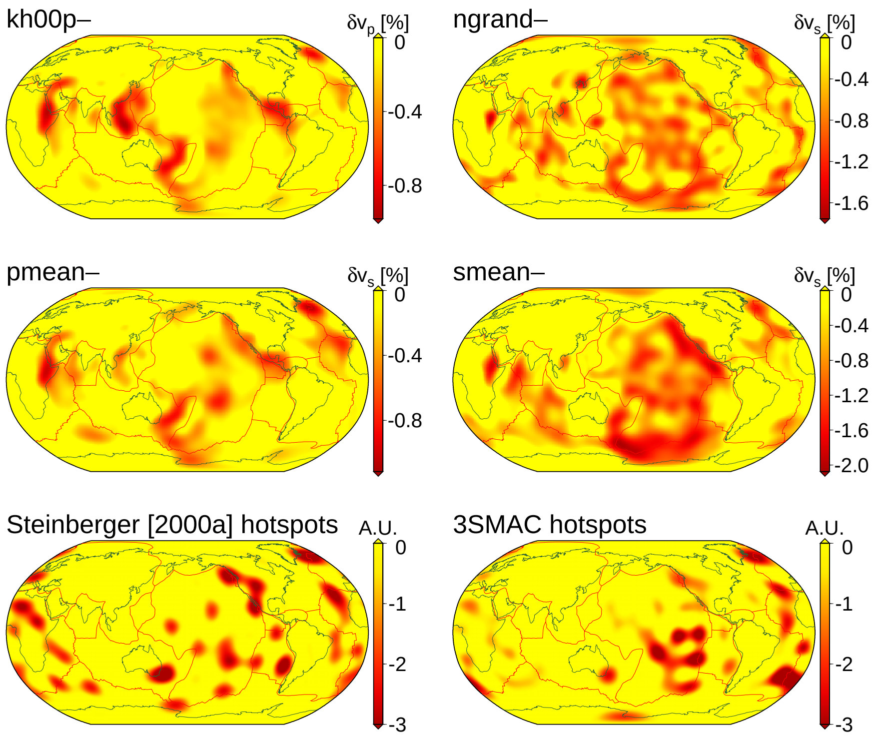

Figure C8. Comparison of negative δv only tomography and hot spot distributions (arbitrary units). The $\ell_{max} = 20$, and depth of tomography is $z = 300$ km. Hot spot fields are based on δ-function expansions of hot spot locations from *Steinberger* [2000a] and 3SMAC [*Nataf and Ricard*, 1996].

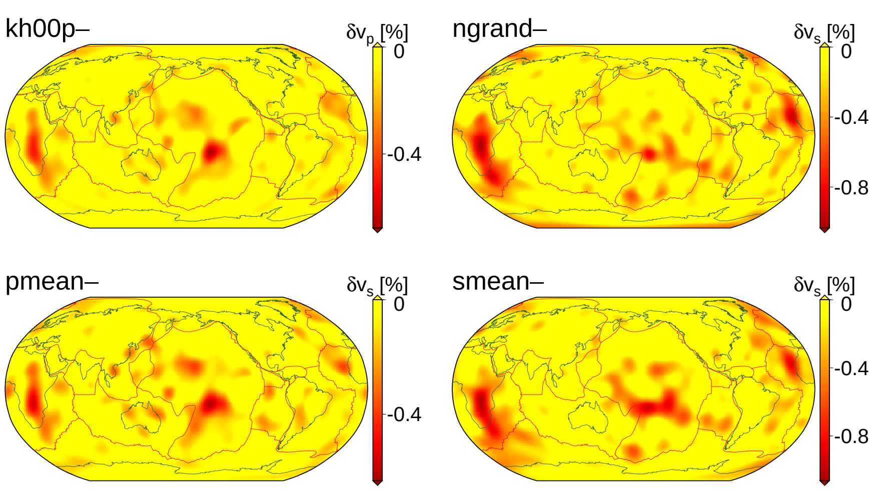

Figure C9. Negative δv only tomography at $z = 1500$ km.

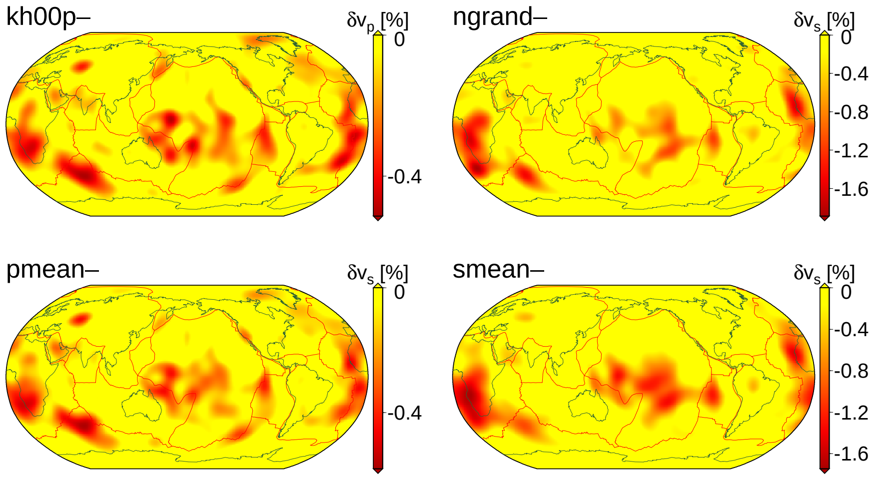

Figure C10. Negative δv only tomography at z = 2500 km.

and Hans-Peter Bunge as well as Bernhard Steinberger and James Kellogg for valuable suggestions on the manuscript. Richard O'Connell, Adam Dziewonski, and Göran Ekström were of great help, offering continuing support and encouragement. Funding for TWB was provided by a DAAD Doktorandenstipendium under the HSP-III program. Most figures were prepared with GMT by *Wessel and Smith* [1991].

References

Anderson, D. L., A seismic equation of state, II, Shear properties and thermodynamics of the lower mantle, *Phys. Earth Planet. Inter.*, *45*, 307–323, 1987.

Anderson, D. L., and A. M. Dziewonski, Upper mantle anisotropy: Evidence from free oscillations, *Geophys. J. R. Astron. Soc.*, *69*, 383–404, 1982.

Antolik, M., G. Ekström, A. M. Dziewonski, Y. J. Gu, J.-F. Pan, and L. Boschi, A new joint *p* and *s* velocity model of the mantle parameterized in cubic B-splines, paper presented at 22nd Annual DoD/DOE Seismic Research Symposium: Planning for Verification of and Compliance with the Comprehensive Nuclear-Test-Ban Treaty (CTBT), New Orleans, La., 2001.

Bergeron, S. Y., D. A. Yuen, and A. P. Vincent, Capabilities of 3-D wavelet transforms to detect plume-like structures from seismic tomography, *Geophys. Res. Lett.*, *27*, 3433–3436, 2000.

Boschi, L., and A. M. Dziewonski, "High" and "low" resolution images of the Earth's mantle — Implications of different approaches to tomographic modeling, *J. Geophys. Res.*, *104*, 25,567–25,594, 1999.

Bunge, H.-P., and S. P. Grand, Mesozoic plate-motion history below the northeast Pacific Ocean from seismic images of the subducted Farallon slab, *Nature*, *405*, 337–340, 2000.

Bunge, H.-P., M. A. Richards, C. Lithgow-Bertelloni, J. R. Baumgardner, S. P. Grand, and B. A. Romanowicz, Time scales and heterogeneous structure in geodynamic earth models, *Science*, *280*, 91–95, 1998.

Castle, J. C., and R. D. van der Hilst, Searching for seismic observations of deep mantle structure, *Eos Trans. AGU*, *81*, Fall Meet. Suppl., F832, 2000.

Christensen, U. R., The influence of trench migration on slab penetration into the lower mantle, *Earth Planet. Sci. Lett.*, *140*, 27–39, 1996.

Čížková, H., O. Čadek, and A. Slancová, Regional correlation analysis between seismic heterogeneity in the lower mantle and subduction in the last 180 Myr: Implications for mantle dynamics and rheology, *Pure Appl. Geophys.*, *151*, 527–537, 1998.

Dahlen, F. A., and J. Tromp, *Theoretical Global Seismology*, Princeton Univ. Press, Princeton, N. J., 1998.

Davies, G. F., Role of the lithosphere in mantle convection, *J. Geophys. Res.*, *93*, 10,451–10,466, 1988.

Davies, G. F., and M. A. Richards, Mantle convection, *J. Geol.*, *100*, 151–206, 1992.

DeMets, C., R. G. Gordon, D. F. Argus, and S. Stein, Current plate motions, *Geophys. J. Int.*, *101*, 425–478, 1990.

Dziewonski, A. M., Mapping the lower mantle: determination of lateral heterogeneity in P velocity up to degree and order 6, *J. Geophys. Res.*, *89*, 5929–5952, 1984.

Dziewonski, A. M., and D. L. Anderson, Preliminary reference Earth model, *Phys. Earth Planet. Inter.*, *25*, 297–356, 1981.

Dziewonski, A. M., B. H. Hager, and R. J. O'Connell, Large scale heterogeneity in the lower mantle, *J. Geophys. Res.*, *82*, 239–255, 1977.

Ekström, G., and A. M. Dziewonski, The unique anisotropy of the Pacific upper mantle, *Nature*, *394*, 168–172, 1998.

Engdahl, E. R., R. D. van der Hilst, and R. Buland, Global teleseismic earthquake relocation with improved travel times and procedures for depth determination, *Bull. Seismol. Soc. Am.*, *88*, 722–743, 1998.

Grand, S. P., Mantle shear structure beneath the Americas and surrounding oceans, *J. Geophys. Res.*, *99*, 11,591–11,621, 1994.

Grand, S. P., R. D. van der Hilst, and S. Widiyantoro, Global seismic tomography; A snapshot of convection in the Earth, *GSA Today*, *7*, 1–7, 1997.

Gu, Y. J., A. M. Dziewonski, W.-j. Su, and G. Ekström, Models of the mantle shear velocity and discontinuities in the pattern of lateral heterogeneities, *J. Geophys. Res.*, *106*, 11,169–11,199, 2001.

Gudmundsson, O., and M. Sambridge, A regionalized upper mantle (RUM) seismic model, *J. Geophys. Res.*, *103*, 7121–7136, 1998.

Hager, B. H., R. W. Clayton, M. A. Richards, R. P. Comer, and A. M. Dziewonski, Lower mantle heterogeneity, dynamic topography and the geoid, *Nature*, *313*, 541–545, 1985.

Inoue, H. Y., Y. Fukao, K. Tanabe, and Y. Ogata, Whole mantle *p* wave travel time tomography, *Phys. Earth Planet. Inter.*, *59*, 294–328, 1990.

Ishii, M., and J. Tromp, Even-degree lateral variations in the earth's mantle constrained by free oscillations and the free-air gravity anomaly, *Geophys. J. Int.*, *145*, 77–96, 2001.

Kárason, H. and R. D. van der Hilst, Constraints on mantle convection from seismic tomography, in *The History and Dynamics of Global Plate Motion*, vol. 121 *Geophys. Monogr. Ser.*, edited by M. R. Richard, R. Gordon, and R. D. van der Hilst, pp. 277–288, AGU, Washington, D.C., 2000.

Kárason, H., and R. D. van der Hilst, Tomographic imaging of the lowermost mantle with differential times of refracted and diffracted core phases (PKP, Pdiff), *J. Geophys. Res.*, *106*, 6569–6588, 2001.

Karato, S.-I., Importance of anelasticity in the interpretation of seismic tomography, *Geophys. Res. Lett.*, *20*, 1623–1626, 1993.

Karato, S.-I., and B. B. Karki, Origin of lateral variation of seismic wave velocities and density in the deep mantle, *J. Geophys. Res.*, *106*, 21,771–21,783, 2001.

Kennett, B. L. N., S. Widiyantoro, and R. D. van der Hilst, Joint seismic tomography for bulk sound and shear wave speed in the Earth's mantle, *J. Geophys. Res.*, *103*, 12,469–12,493, 1998.

Lithgow-Bertelloni, C., and M. A. Richards, Cenozoic plate driving forces, *Geophys. Res. Lett.*, *22*, 1317–1320, 1995.

Lithgow-Bertelloni, C., and M. A. Richards, The dynamics of Cenozoic and Mesozoic plate motions, *Rev. Geophys.*, *36*, 27–78, 1998.

Lithgow-Bertelloni, C., M. A. Richards, Y. Ricard, R. J. O'Connell, and D. C. Engebretson, Toroidal-poloidal partitioning of plate motions since 120 Ma, *Geophys. Res. Lett.*, *20*, 375–378, 1993.

Masters, G., H. Bolton, and G. Laske, Joint seismic tomography for p and s velocities: How pervasive are chemical anomalies in the mantle?, *Eos Trans. AGU*, *80*(17), Spring Meet. Suppl., S14, 1999.

Masters, G., T. H. Jordan, P. G. Silver, and F. Gilbert, Aspherical Earth structure from fundamental spheroidal-mode data, *Nature*, *298*, 609–613, 1982.

Masters, G., G. Laske, H. Bolton, and A. M. Dziewonski, The relative behavior of shear velocity, bulk sound speed, and compressional velocity in the mantle: Implications for chemical and thermal structure, in *Earth's Deep Interior: Mineral Physics and Tomography From the Atomic to the Global Scale*, vol. 117 *Geophys. Monogr. Ser.*, edited by S.-I. Karato, A. M. Forte, R. C. Liebermann, G. Masters, and L. Stixrude, pp. 63–87, AGU, Washington, D.C., 2000.

Mégnin, C., and B. Romanowicz, The effects of the theoretical formalism and data selection on mantle models derived from waveform tomography, *Geophys. J. Int.*, *138*, 366–380, 1999.

Mégnin, C., and B. Romanowicz, The shear velocity structure of the mantle from the inversion of body, surface, and higher modes waveforms, *Geophys. J. Int.*, *143*, 709–728, 2000.

Mitrovica, J. X., and A. M. Forte, Radial profile of mantle viscosity: Results from the joint inversion of convection and postglacial rebound observables, *J. Geophys. Res.*, *102*, 2751–2769, 1997.

Nataf, H.-C., and Y. Ricard, 3SMAC: an a priori tomographic model of the upper mantle based on geophysical modeling, *Phys. Earth Planet. Inter.*, *95*, 101–122, 1996.

Oganov, A. R., J. P. Brodholt, and G. D. Price, The elastic constants of $MgSiO_3$ perovskite at pressures and temperatures of the Earth's mantle, *Nature*, *411*, 934–937, 2001.

Press, W. H., S. A. Teukolsky, W. T. Vetterling, and B. P. Flannery, *Numerical Recipes in C: The Art of Scientific Computing*, 2nd ed., Cambridge Univ. Press, New York, 1993.

Puster, P., and T. H. Jordan, How stratified is mantle convection?, *J. Geophys. Res.*, *102*, 7625–7646, 1997.

Ray, T. R., and D. L. Anderson, Spherical disharmonics in the Earth sciences and the spatial solution: Ridges, hotspots, slabs, geochemistry and tomography correlations, *J. Geophys. Res.*, *99*, 9605–9614, 1994.

Ricard, Y., M. A. Richards, C. Lithgow-Bertelloni, and Y. Le Stunff, A geodynamic model of mantle density heterogeneity, *J. Geophys. Res.*, *98*, 21,895–21,909, 1993.

Richards, M. A., B. H. Hager, and N. H. Sleep, Dynamically supported geoid highs over hotspots: Observation and theory, *J. Geophys. Res.*, *93*, 7690–7708, 1988.

Ritsema, J., and H. J. van Heijst, Seismic imaging of structural heterogeneity in Earth's mantle: Evidence for large-scale mantle flow, *Sci. Progr.*, *83*, 243–259, 2000.

Ritsema, J., H. J. van Heijst, and J. H. Woodhouse, Complex shear wave velocity structure imaged beneath Africa and Iceland, *Science*, *286*, 1925–1928, 1999.

Ritzwoller, M. H., and E. M. Lavely, Three dimensional models of the Earth's mantle, *Rev. Geophys.*, *33*, 1–66, 1995.

Robertson, G. S., and J. H. Woodhouse, Ratio of relative S to P velocity heterogeneity in the lower mantle, *J. Geophys. Res.*, *101*, 20,041–20,052, 1996.

Saltzer, R. L., R. D. van der Hilst, and H. Kárason, Comparing P and S wave heterogeneity in the mantle, *Geophys. Res. Lett.*, *28*, 1335–1338, 2001.

Steinberger, B., Plumes in a convecting mantle: Models and observations for individual hotspots, *J. Geophys. Res.*, *105*, 11,127–11,152, 2000a.

Steinberger, B., Slabs in the lower mantle — Results of dynamic modelling compared with tomographic images and the geoid, *Phys. Earth Planet. Inter.*, *118*, 241–257, 2000b.

Steinberger, B., and R. J. O'Connell, Advection of plumes in mantle flow: Implications for hotspot motion, mantle viscosity, and plume distribution, *Geophys. J. Int.*, *132*, 412–434, 1998.

Su, W.-J., and A. M. Dziewonski, Predominance of long-wavelength heterogeneity in the mantle, *Nature*, *352*, 121–126, 1991.

Su, W.-J., and A. M. Dziewonski, On the scale of mantle heterogeneity, *Phys. Earth Planet. Inter.*, *74*, 29–45, 1992.

Su, W.-J., and A. M. Dziewonski, Simultaneous inversion for 3-D variations in shear and bulk velocity in the mantle, *Phys. Earth Planet. Inter.*, *100*, 135–156, 1997.

Tackley, P. J., Effects of strongly variable viscosity on three-dimensional compressible convection in planetary mantles, *J. Geophys. Res.*, *101*, 3311–3332, 1996.

Tackley, P. J., Mantle convection and plate tectonics: Toward an integrated physical and chemical theory, *Science*, *288*, 2002–2007, 2000.

van der Hilst, R. D., and H. Kárason, Compositional heterogeneity in the bottom 1000 kilometers of Earth's mantle: Toward a hybrid convection model, *Science*, *283*, 1885–1887, 1999.

van der Hilst, R. D., S. Widiyantoro, and E. R. Engdahl, Evidence of deep mantle circulation from global tomography, *Nature*, *386*, 578–584, 1997.

Wessel, P., and W. H. F. Smith, Free software helps map and display data, *Eos Trans. AGU*, *72*, 445–446, 1991.

Wortel, M. J. R., and W. Spakman, Subduction and slab detachment in the Mediterranean-Carpathian region, *Science*, *209*, 1910–1917, 2000.

Zhong, S., and M. Gurnis, Mantle convection with plates and mobile, faulted plate margins, *Science*, *267*, 838–842, 1995.

Zhong, S., M. T. Zuber, L. Moresi, and M. Gurnis, Role of temperature-dependent viscosity and surface plates in spherical shell models of mantle convection, *J. Geophys. Res.*, *105*, 11,063–11,082, 2000.